Anna Weitzer, BSc

Melting of Lipid Domains in Four Component Mixtures

Master's Thesis

For obtaining the academic degree of

Diplom-Ingenieurin

Master's degree programme: Technical Physics

Graz University of Technology

Supervisor:
Assoc.-Prof. Dr. Georg Pabst

Institute of Materials Physics

in cooperation with:
Institute of Molecular Biosciences, University of Graz

Graz, July 2016

EIDESSTATTLICHE ERKLÄRUNG

AFFIDAVIT

Ich erkläre an Eides statt, dass ich die vorliegende Arbeit selbstständig verfasst, andere als die angegebenen Quellen/Hilfsmittel nicht benutzt, und die den benutzten Quellen wörtlich und inhaltlich entnommenen Stellen als solche kenntlich gemacht habe. Das in TUGRAZonline hochgeladene Textdokument ist mit der vorliegenden Dissertation identisch.

I declare that I have authored this thesis independently, that I have not used other than the declared sources/resources, and that I have explicitly indicated all material which has been quoted either literally or by content from the sources used. The text document uploaded to TUGRAZonline is identical to the present doctoral dissertation.

—————————————————   —————————————————————
Datum / Date   Unterschrift / Signature

Abstract

Membranes, as they occur in mammalian cells, are as interesting as they are complex. Therefore, simple models have to be found to understand their behavior and subsequently use this knowledge for various health applications such as drug therapy. Building artificial membranes of lipid-only systems to study their properties under controlled and simplified conditions is a well-established method in the field of biophysics. This contribution focusses on DSPC/DOPC/POPC/Cholesterol mixtures, which generate domain structures of coexisting liquid-ordered (L_o) and liquid-disordered (L_d) phases. The first aspect investigated was the dependence of the domain size on the DOPC/POPC ratio, particularly the transition from macroscopic to nanoscopic domains with increasing POPC content. Small Angle X-ray Scattering (SAXS) data were collected at different synchrotron facilities and further analyzed with two recently developed global analysis programs for multilamellar vesicles. This novel approach allows for parameters such as the bilayer thicknesses and the bending fluctuations to be determined. Secondly, SAXS and Differential Scanning Calorimetry (DSC) measurements monitored the temperature dependence of the transition between a domain structure (phase separation) and a homogeneous L_d phase. These data provide insight into the melting of L_o domains, showing a dependence of the transition temperature on the DOPC/POPC ratio. Notably, a shift to higher temperatures with increasing DOPC content is observed. Furthermore, our data suggest that the critical behavior follows a 2-dimensional Ising Model.

Kurzfassung

Membranen, wie sie beispielsweise in Säugetierzellen vorkommen, sind ein gleichsam interessantes wie komplexes Gebiet. Daher müssen einfache Modelle gefunden werden, um ihr Verhalten zu verstehen und in weiterer Folge dieses Wissen für verschiedene Anwendungen im Gesundheitsbereich, wie medikamentöse Behandlungen, nutzen zu können.

Die Herstellung künstlicher Zellmembranen aus reinen Lipid-Systemen, um ihre Eigenschaften unter kontrollierten und vereinfachten Bedingungen studieren zu können, ist eine bewährte Methode im Bereich der Biophysik. Dieser Beitrag beschäftigt sich mit DSPC/DOPC/POPC/Cholesterol-Systemen, welche eine Domänenstruktur aus koexistierenden flüssig geordneten (L_o) und ungeordneten (L_d) Phasen bilden.

Der erste untersuchte Aspekt behandelt die Abhängigkeit der Domänengröße vom DOPC/POPC-Verhältnis, insbesondere den Übergang von makroskopischen zu nanoskopischen Domänen mit steigendem POPC-Gehalt. Die Daten aus Kleinwinkel-Röntgenstreumessungen (SAXS) wurden an verschiedenen Synchrotron-Einrichtungen aufgenommen und anschließend mit zwei kürzlich entwickelten, globalen Analyseprogrammen für multilamellare Vesikel analysiert. Dieser neue Ansatz erlaubt die Bestimmung von Parametern wie den Lipid-Doppelschicht-Dicken oder den Biege-Fluktuationen.

Zweitens zeigten SAXS und Dynamische Differenzkalorimetrie (DSC) Messungen die Temperaturabhängigkeit des Übergangs zwischen der phasenseparierten Domänenstruktur und einer homogenen L_d-Phase. Diese Daten geben Einblick in das Schmelzen von L_o-Domänen, wobei eine Abhängigkeit der Übergangstemperatur vom DOPC/POPC-Verhältnis festgestellt wurde. Dabei war eine Verschiebung hin zu höheren Temperaturen mit steigendem DOPC-Gehalt zu beobachten. Des weiteren suggerieren unsere Daten, dass das kritische Verhalten der Lipid-Doppelschicht-Dicken unterhalb der Übergangstemperatur einem 2-dimensionalen Ising-Modell folgt.

Contents

List of Tables

List of Figures

Acknowledgements

First of all, I would like to thank my supervisor Georg Pabst for introducing me into the field of Biophysics, for his support and for giving me the chance to do experiments in different countries and to collaborate with international people. I would also like to thank Karl Lohner for his help and interest in my research, particularly concerning chemical issues and techniques. Furthermore, I want to thank the whole team, especially Drew, Michal, Peter, Benjamin, Barbara and Santosh, for their assistance, many good discussions and a very enjoyable working atmosphere with a great social cohesion. I would also like to thank my boyfriend Ben, my parents and my friends for their encouragement, for spiriting me up when I needed it and for always giving me their unconditional backup.

Chapter 1

Introduction

1.1 Cells

Cells are the most basic form of life and constitute the structural and functional elements of all living organisms as they are the smallest self-preserving units that can replicate independently. They are composed of organic molecules, carbon containing compounds that can be classified into 4 important categories: sugars, amino acids, nucleotides and fatty acids. Figure 1.1 illustrates a model of a eukaryotic cell.
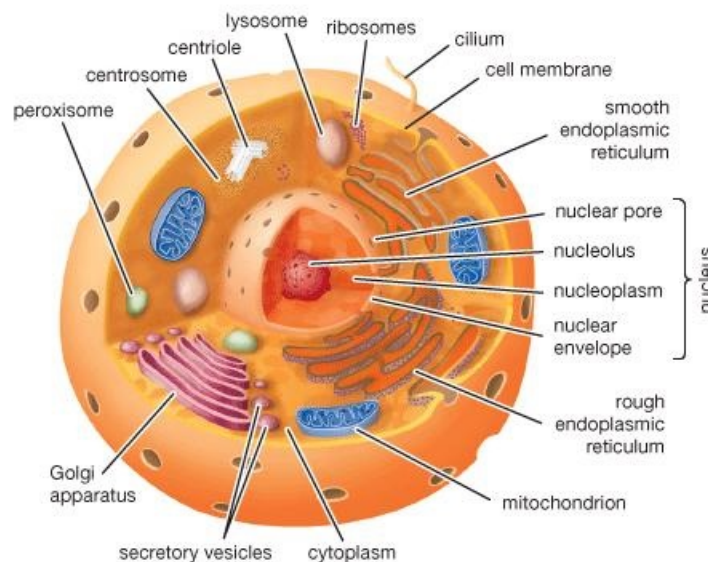
Figure 1.1: Eukaryotic cell (Adapted from [1])

Eukaryotic cells mainly consist of cytoplasm, a structure building the interior of the cell with a liquid part called cytosol and a solid part, the cytoskeleton. Imbedded in this medium are several different organelles. They include the cell nucleus, that contains the DNA, the mitochondria, the endoplasmic reticulum, eventually with ribosomes, the golgi apparatus, the lysosomes and the vacuoles (all outlined in Figure 1.1). But the focus of this thesis was, arguably the most important organelle, the cell membrane, which is the semi-permeable barrier separating the other elements from their environment.

1.1.1 The cell membrane

Cell membranes are not only a delimitation between the different cells or a divide between cellular compartments, but a highly complex construct with a hierarchical organization that contains over 1000 different lipid species, proteins and steroids. The total area of membranes in the human body has been estimated to about 100 km^2 [22]. A widely-used model for the membrane structure is the so-called **"fluid mosaic model"** developed by S.J.Singer and G.Nicolson in 1972 [36], where the proteins build a structure comparable to a mosaic in the liquid crystalline lipid bilayer (as illustrated in Figure 1.2). Thereby the proteins can be located on the surface of the membrane (extrinsic proteins) or in the interior (intrinsic proteins). The heterogeneity of the lipids is not considered in this model.

Another model that incorporates the presence of different lipids is the lipid/protein domain model by Shimshick and McConnell from 1973. It contains lipid phase separation due to the various occurring membrane lipids [34]. Nevertheless, the fluid mosaic is still the most widely used model.
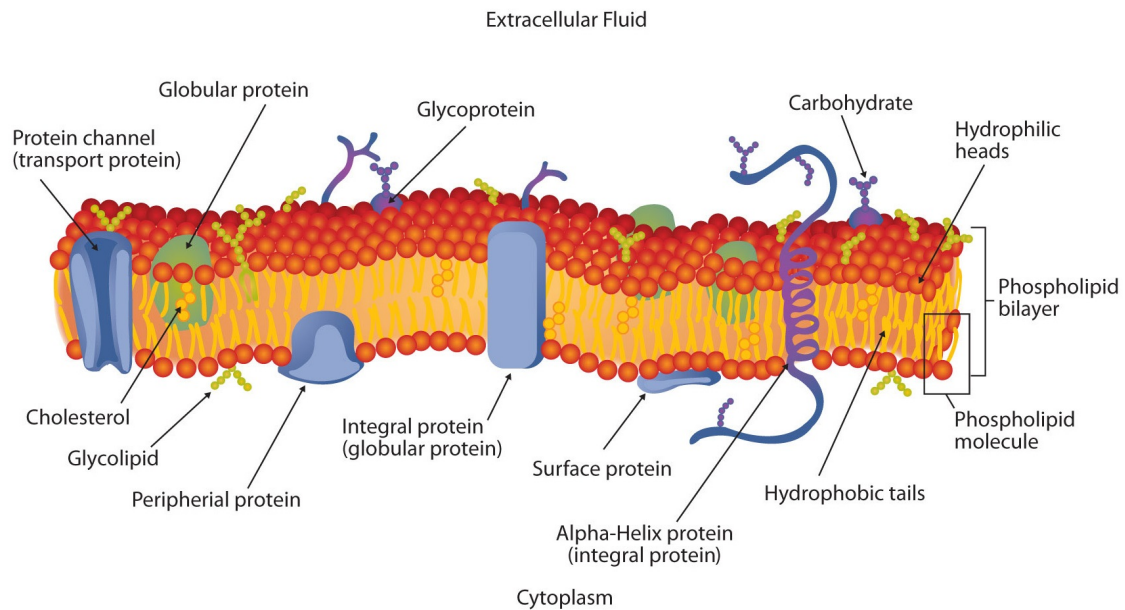
Figure 1.2: Illustration of the plasma membrane in the fluid mosaic model (Adapted from [5])

Naturally occurring membranes are thin (in the range of only 4-5 nanometers), flexible and of liquid consistency. Cellular membranes are highly selective as they are basically permeable to water but impenetrable for ions and polar molecules. Transport of selected ions and molecules can take place via special protein channels. Natural membranes have an asymmetric distribution of lipids [20]. In other words, the lipids on the inner and the outer monolayer differ. The asymmetric nature of the membrane is further demonstrated through special transport systems that only work in one direction (for example the transport of Na^+ out of and Ka^- into the cell). For details on lipid bilayers and how they form, see chapters 1.2.2 and 1.3.

The most important lipid bilayer is the **plasma membrane (PM)**. It can be imagined as a 2-dimensional solution of lipids, proteins and steroids. The PM forms the outside of all living cells and gives them their individuality due to the innumerable

variations of different compositions. Also there are various oligosaccharide groups on the outer side of the membrane that play an important role in cell recognition, the building of multi-cellular structures and consequently the formation of different kinds of tissues. The plasma membrane has many functions as it regulates different cellular processes, like cell adhesion, ion conductivity and cell signaling.

There are different forces occurring in cell membranes. First of all, the Van der Waals forces, caused by fluctuations of the electric dipole moments. Additionally to that, there are electrostatic and double layer forces. They can all be summarized in the DLVO theory [39]. Furthermore, there are structure forces, thermal fluctuation forces, directional entropic forces, sterical forces and bridge forces coming from polymerical components of biological membranes [29].

1.2 Lipids

Lipids are oily, organic compounds. They are amphiphatic molecules, in other words they possess both hydrophobic and hydrophilic character. Their biological functions are mainly their occurance in membranes, their use for energy storage and their contribution to signaling processes among others. Their composition is not genetically determined but develops from enzymatic reactions and metabolism.

Figure 1.3 gives an overview on the lipid categories occurring in living systems.
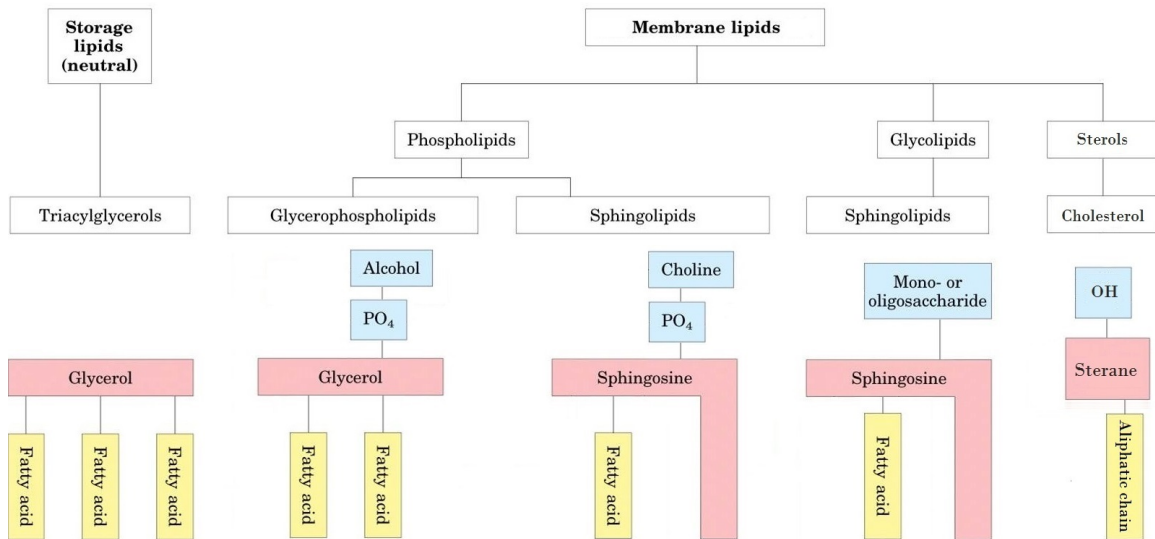
Figure 1.3: Lipid categories in living systems (Adapted from [18])

1.2.1 Fatty acids

Characteristic components in most lipids are the fatty acids. These are organic acids with 2 to 36 (most common are those with 14-22) C-atoms. They consist of a carboxylic acid group and a long non-polar hydrocarbon chain [19]. The chains can be saturated (only single bonds) or unsaturated (contain one or more double bonds) which makes them locally more rigid because they are not as free to rotate as the single bonds at the C-C-bond. Overall double bonds increase the disorder in the bulk. The melting behavior and the solubility depend strongly on the length of the chains and the number of double bonds. With increasing length of the hydrocarbon chains the fatty acids get less soluble in water and their melting point shifts to higher temperatures because of the van der Waals forces between them. The more unsaturated the chains are, the lower the melting point, especially for cis-double bonds as they cause kinks in the structure of the chains. Figure 1.4 compares the structures of saturated and (cis-)unsaturated fatty acids on examples.
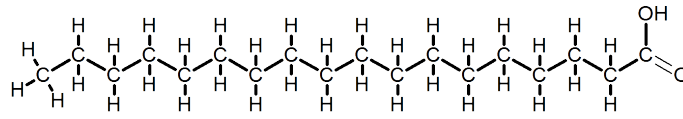
Saturated Fatty Acid
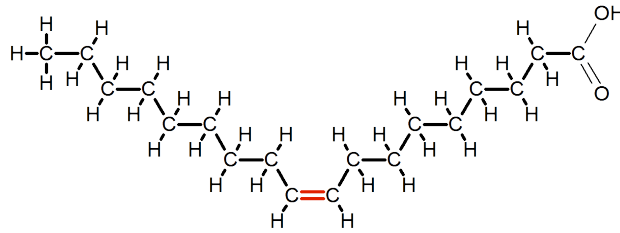
Unsaturated Fatty Acid

Figure 1.4: Saturated and unsaturated fatty acids

Innumerable different fats can be built based on fatty acids. The most important categories in the field of biological membranes are the polar lipids which are briefly described in the following (1.2.2 - 1.2.3).

1.2.2 Glycerophospholipids

An important group of membrane lipids are the glycerophospholipids. They belong to the group of diacylglyceroles. Figure 1.5 shows their fundamental composition.
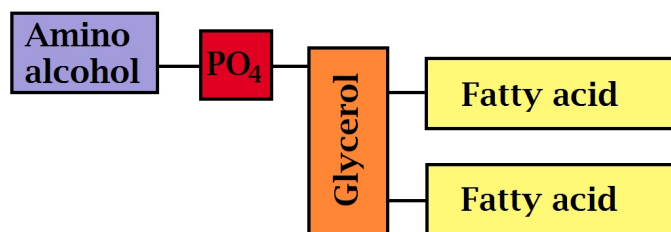
Figure 1.5: Structure of glycerophospholipids

They consist of an amino alcohol group, a phosphate group, a glycerol group and two fatty acid chains. Phospholipids are amphiphilic, which means they have hydrophilic, polar headgroups and hydrophobic, apolar tails.

There are certain glycerophospholipids that occur very often in mammalian cells; their structures are shown in Figure 1.6.

Figure 1.6: Overview over some important glycerophospholipids (Adapted from [3])

The glycerophospholipids used in this work were 1,2-Distearoyl-sn-glycero-3-phosphocholine (DSPC), 1,2-Dioleoyl-sn-glycero-3-phosphocholine (DOPC) and 1-Palmitoyl-2-oleoyl-sn-glycero-3-phosphorylcholine (POPC). Their structures can be seen in Figure 1.7.
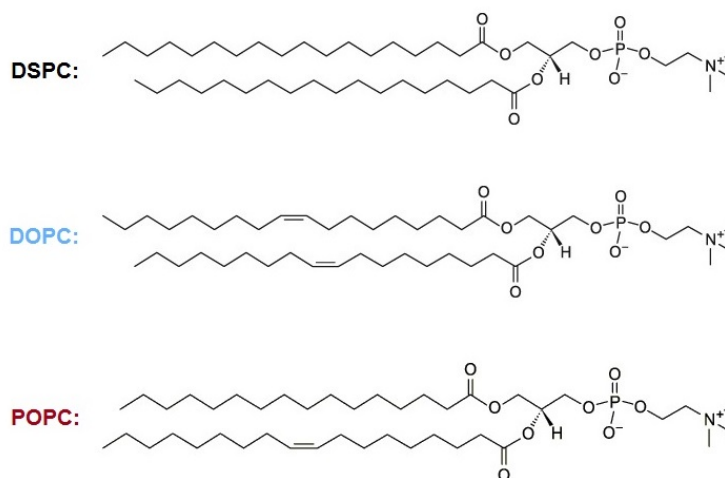
Figure 1.7: Chemical structures of DSPC, DOPC and POPC

DSPC is a high-melting lipid with a transition temperature, of 55°C for the transition from gel to fluid phase, whose fatty acid chains only contain single bonds. POPC and DOPC, with one and two double bonds in their chains, are low-melting lipids with transition temperatures of -2°C and -17°C. Transition temperatures were adopted from the Avanti website.[1]

Self-assembly

The amphiphilic nature of these lipids allows them to self-assemble depending on their surrounding environment. Contingent on the type of buffer there are different structural forms they can arrange into. The lipids align in such a way as to minimize the free energy which is achieved by the aversion of contact between the hydrophobic chains and the buffer (that is usually water as the biological solvent). What happens during the process of self-assembly can be described as a 3-dimensional aggregation.

---

[1]www.avantilipids.com

It only occurs when the lipid concentration in the buffer is at or above the critical aggregation concentration (cac).

The size of the built aggregates depends on the following equation [25]:

$$\mu_N^0 = \mu_\infty^0 + \frac{\alpha k_B T}{N^P} \tag{1.1}$$

μ_N^0 is the chemical standard potential (the mean free energy of the interactions per molecule in the aggregate) with N the aggregation number (number of monomers). μ_∞^0 stands for the standard chemical potential of an infinite number of monomers. $\alpha k_B T$ is the monomer-monomer binding energy and P represents the inverse dimension. If $\mu_N^0 < \mu_1^0$, aggregates with a size of N monomers are built.

The form of the aggregates is also conditioned by the temperature and the shape of the molecules which is defined by the form parameter P:

$$P = \frac{v}{al} \tag{1.2}$$

v gives the volume of the chains, a the area of the head group and l stands for the length of the hydrocarbon chains.

The different structures can be seen in Figure 1.8.
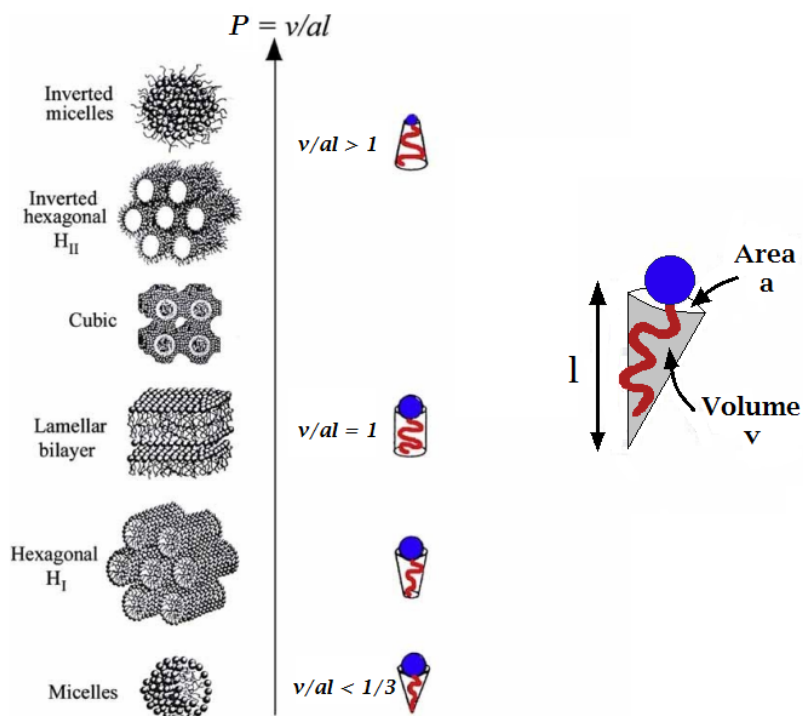
Figure 1.8: Structures of self-assembled lipids depending on the form parameter P (Adapted from [23])

The figure illustrates self-assembled structures for lipids of differing molecular shapes including cones, inverted cones and cylinders, but the structures are also concentration dependent. The aggregate structures examined in this work are the bilayers in liposomes/vesicles (Fig.1.9). Lamellar bilayers form at small values of P and at low lipid concentrations.

As a lamellar bilayer the tails are protected from the polar buffer on the outside as well as on the inside by deforming into a closed surface. (More details on the lipid bilayer can be found in section 1.3.)

Liposomes are a useful tool for drug delivery as both hydrophobic (within the bilayer) and hydrophilic (inside the vesicle) drugs can be transported and brought to the desired area of the body. They can also be used in diagnostics for infiltrating marker
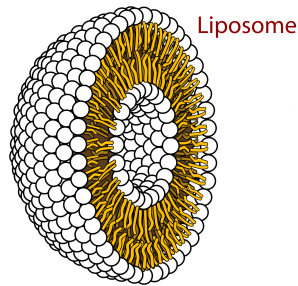
Figure 1.9: Structure of a liposome in a polar buffer

molecules.

1.2.3 Sphingolipids

Like glycerophospholipids, sphingolipids have polar head groups and 2 non-polar chains but they are lacking of glycerol. They contain one molecule of a long-chained fatty acid, one molecule of the long-chained amino-alcohol sphingosine or a sphingosine derivate and a polar head-alcohol [19].

There are three categories of sphingolipids: Sphingomyelins, cerebrosides and gangliosides of which only the first contain phosphorus. Therefore, sphingomyelin (SM) can also be counted as a phospholipid. Comparing SM, the most important sphingolipid in cell membranes, to phosphoglycerides like PE or PC, it shows quite similar characteristics. For the structures of sphingosine and sphingomyelin see Fig.1.10.
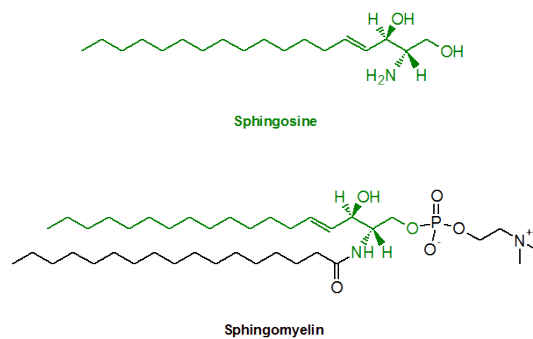
Figure 1.10: Structures of sphingosine and sphingomyelin

1.2.4 Sterol lipids

For mammalian cell membranes the most important steroid is cholesterol because it is quite common and has a major influence on the behavior of other lipids. Cholesterol is a precursor for other important steroid molecules: the bile salts, steroid hormones, and vitamin D to name but a few [38]. As a small, rigid molecule cholesterol can move through the membrane and modulate its physical properties; for example it is an important factor for the regulation of membrane fluidity. High cholesterol contents suppress the gel formation of the phospholipid membrane by disordering them, but can induce a higher structural order to the liquid crystalline phase, whereby the membrane becomes more stable [40]. (For more details about phases see section 1.4.) Another function of cholesterol is the metabolism of proteins and the lateral organization of lipids within the membrane [13].
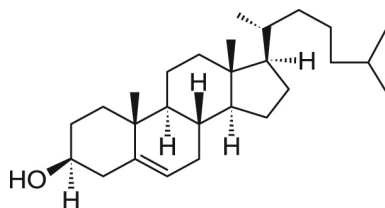
Figure 1.11: Structure of cholesterol

Figure 1.11 shows the steroid-ring-structure of cholesterol with a single OH-group as the polar head and a short hydrocarbon-chain.

The concentration of cholesterol in the individual cells can be regulated by the body so that the membrane can be adjusted to outer influences like changing temperatures. The content of cholesterol in animal plasma membranes lies between 20% and 50% [22]. The membranes of the cell organelles on the contrary only contain a few percent of cholesterol and prokaryotes - cells without real nucleus (like bacteria) - usually do not contain cholesterol at all.

1.3   Lipid bilayers

In our simplified model of a cellular plasma membrane only a select number of lipids are chosen. Lipid membranes are considered soft matter as there are no strong chemical bonds between the molecules. Figure 1.12 shows an illustration of a bilayer considering the heterogeneity of the lipids and also the asymmetry on the outer and inner monolayer.
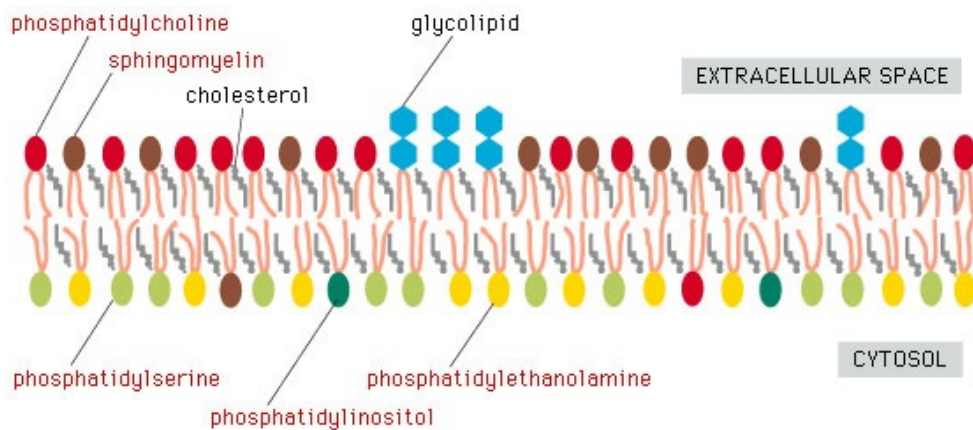
Figure 1.12: Example of a lipid bilayer (Adapted from [4])

Membranes are dynamic systems, as the lipids can undergo several movements which occur at different time scales (between 10^{-11} and a few seconds). They are schematically illustrated in Figure 1.13.

Another occurring dynamic process is the transverse diffusion between the monolayers, also called "flip-flop". As transverse lipid relocation is energetically unfavorable, it is a relatively slow process, taking place from a few seconds up to weeks. Figure 1.14 illustrates the transaction.
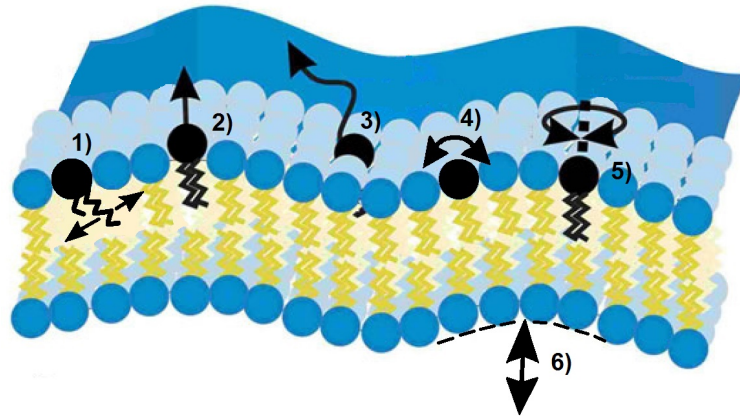
Figure 1.13: Dynamic processes within the membrane (Adapted from [28])
1) conformational transition of the chains or defect movement
2) vertical vibrations or protrusion
3) lateral diffusion
4) head group movement
5) rotational diffusion
6) collective undulation movement
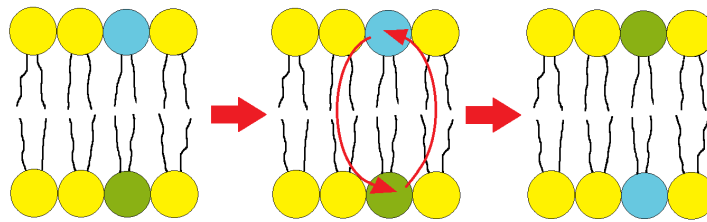
Figure 1.14: Transverse diffusion (flip-flop)

Lipid bilayers form multilamellar vesicles (MLVs) where multiple bilayers are interlaced in a spherical structure with water layers in between (see Figure 1.15a) or unilamellar vesicles (ULVs) (Figure 1.15b), where there's only one bilayer building the surface of the liposome and water in the middle.
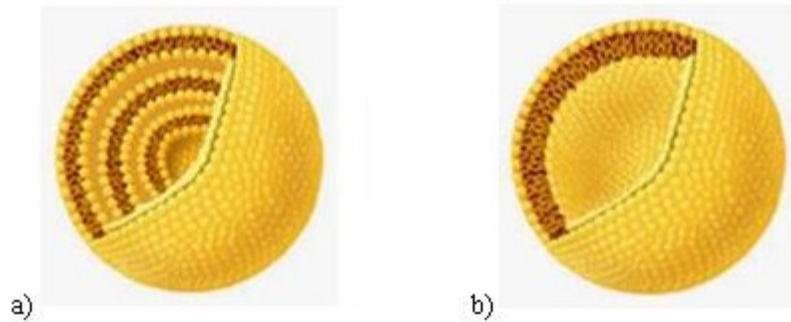
Figure 1.15: a) multilamellar b) unilamellar vesicles (Adapted from [37])

A more detailed description of two bilayers and an intermediate water layer is given in Figure 1.16. "d" stands for the d-spacing, which is the distance between the beginning of one bilayer and the next, "d_W" is the thickness of the water layer between the bilayers, "d_B" the bilayer thickness (d_B = d - d_W). The plot on the right shows the corresponding **electron density profile**.
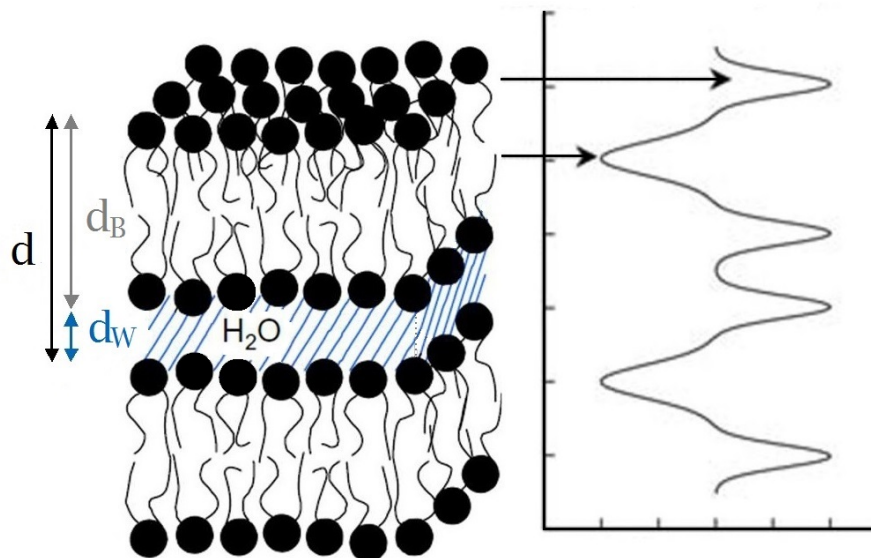
Figure 1.16: Illustration of two lipid bilayers and an intermediate water layer with an electron density profile on the right, where the electron density is plotted depending on the position within the bilayer (Adapted from [10])

The profile illustrated in Figure 1.16 shows regions of high electron density in the area of the head groups and reaches a minimum for the more mobile (less dense) terminal methyl groups. Electron density profiles can be determined from X-ray scattering data by performing Fourier transformations on the scattered intensities as it is shown in the equations below (Eq.1.3 - Eq.1.5) [**?**].

The form factor F(q), which is the amplitude of the scattered wave (q stands for the wave vector), is the sum of the coherent scattering length b^{coh} of all atoms in the sample (Equation 1.3). The right side of the equation describes the continuous case which is the integral over $\rho(\mathbf{r})$, the scattering length density, for the whole sample volume.

$$F(\mathbf{q}) = \sum_{j}^{atoms} b_j^{coh} e^{i\mathbf{q}\cdot r_j} = \int^{sample\ volume} \rho(\mathbf{r})e^{i\mathbf{q}\cdot\mathbf{r}}d\mathbf{r} \tag{1.3}$$

The form factor is proportional to the observed intensity of the scattered wave (see Eq.1.4).

$$I(\mathbf{q}) \propto |F(\mathbf{q})|^2 S_p(\mathbf{q}) \tag{1.4}$$

$S_p(\mathbf{q})$ stands for the inter-particle structure factor which describes the relative positions of particles. The scattering length density can be determined from the form factor via Fourier transformation, as it is shown in Eq.1.5.

$$\rho(r) = \int F(\mathbf{q})e^{-i\mathbf{q}\cdot r}d\mathbf{q} \tag{1.5}$$

Some regions of the lipid bilayer experience high lateral pressures; the **lateral pressure profile** can be seen in Figure 1.17.
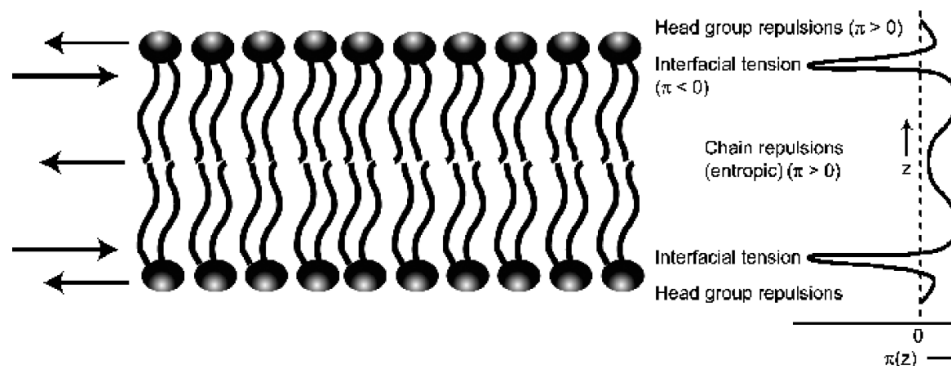
Figure 1.17: Lipid bilayer with lateral pressure profile (Adapted from [22])

The lateral pressure profile consists of 3 different parts. Firstly, a positive pressure arising from the repulsive forces between the head groups because of entropic and electrostatic interactions. Then there is a negative pressure at the hydrophobic-hydrophilic interface because contact of water with the non-polar areas is energetically unfavorable and therefore avoided by a strong attraction minimizing it (hydrophobic effect). The third part is a positive pressure from the repulsion between the chains caused by entropic forces during collisions.

Changes in the lateral pressure can alter the conformation of membrane proteins and therefore influence their function. Lateral pressure profiles are experimentally inaccessible so far but theoretically they can be gained by molecular dynamic (MD) simulations [25].

The **thickness of a lipid membrane** depends on different factors: firstly, the length and degree of saturation of the fatty-acid chains. Bilayer thickness increases with fatty acid chain length and with the degree of carbon-carbon-bond saturation. Bilayer thickness also depends inversely on the degree of hydration (thickness increases with lower hydration). Cholesterol also strongly influences the thickness as it has an ordering effect on the chains of the phospholipids and thereby usually thickens the bilayer. A last important factor is temperature. Basically it can be said that the higher the temperature is, the thinner the bilayer gets but there is an exception at the so-called main-phase-transition where the thickness of the bilayer changes abruptly because the system changes its order by turning into another state [22]. (Phases are described in the next chapter.)

1.4 Phase behavior of different mixtures

Mixtures of lipids in lamellar structures build different phases depending on temperature and composition. At low temperatures the gel phase L_β is built, which is characterized by a high ordering of the fatty acid chains. At higher temperatures the gel phase undergoes a first order melting transition into the liquid disordered phase L_d. Thereby the chains need a larger conformation space, the 2-dimensional long range order is lost and the lipid lateral diffusion is increased [7]. In the presence of cholesterol another fluid phase exists, the liquid ordered phase L_o. Due to cholesterol's propensity to increase the order of the lipids, L_o takes on characteristics of both, the gel-phase L_β and the liquid disordered phase L_d. For example, L_o has an absence of 2-dimensional ordering in the bilayer plane, like L_d, but has a high degree of chain ordering along the hydrocarbon chains and the lipid lateral diffusion is rel-

atively fast [7]. The impact of cholesterol on the bilayer is called condensing effect. Thereby the chains of the phospholipids are aligned perpendicular to the bilayer plane, which results in a thickened bilayer, and the distance between the headgroups of the phospholipids to be increased. Thus the properties of the membrane are changed; the mechanical strength is increased, the water permeability is reduced and the membrane fluidity is decreased [10]. There are different explanations for the interaction of cholesterol with the lipids, such as the superlattice model, the condensed complex model or the most common one, the umbrella model [10]. When a low-melting lipid, a high-melting lipid and cholesterol are mixed, the L_d phase typically contains most of the low-melting lipid, whereas the L_o areas are enriched in high-melting lipid and cholesterol as it favors to pack with saturated lipids. At high temperatures the L_o phase melts into a pure L_d phase [21]. A comparison of the structures of the fluid phases can be seen in Figure 1.18.
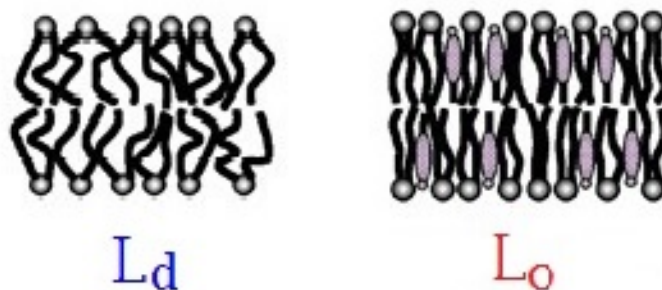
Figure 1.18: Structures of the liquid disordered phase L_d (left) and the liquid ordered phase L_o (right) (Adapted from [6])

The appearance of the different phases depends, as already mentioned above, on the composition and the temperature as shown in the phase diagram in Figure 1.19.
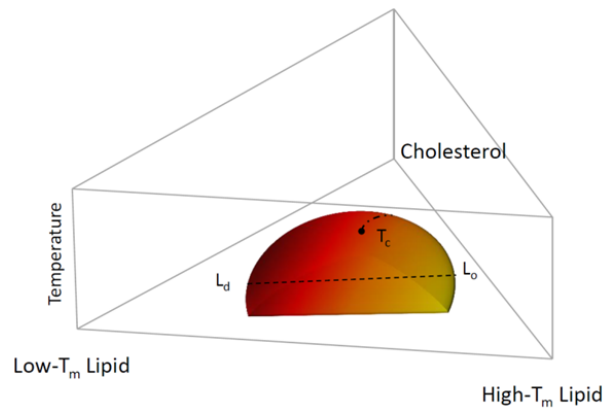
Figure 1.19: Phase diagram of a 3-component lipid mixture depending on composition and temperature (Adapted from [21])

The phase diagram for a lipid with a high melting temperature, a lipid with a low melting temperature and cholesterol shows, that the region of phase coexistence becomes smaller with increasing temperature, until at a certain point, the critical temperature, the liquid ordered phase melts into a liquid disordered phase.

At a constant temperature the occurrence of the different phases only depends on the composition as shown in the compositional phase diagram of the quarternary mixture DSPC/DOPC/POPC/Cholesterol for a given temperature in Figure 1.20.
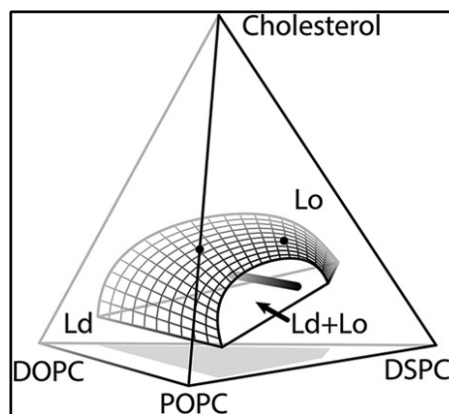
Figure 1.20: Phase diagram of a DSPC/DOPC/POPC/Cholesterol mixture (Adapted from [8])

The figure shows different areas of pure liquid ordered and liquid disordered phases as well as coexisting areas. The demixing of the phases takes place along the tielines, the composition of the liquid ordered and liquid disordered phases can be read from the tieline endpoints. The lateral arrangement of the coexisting phases into a domain structure is the topic of section 1.5.

1.5   Domains and Rafts

Lipid **domains** are membrane inhomogeneities of coexisting liquid ordered and liquid disordered phases that are laterally phase separated. Figure 1.21 shows a fluorescent microscopic image of domains in the order of a few μm.
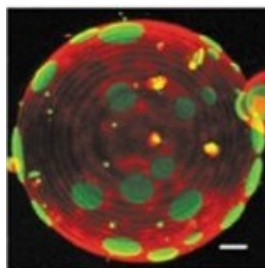
Figure 1.21: Fluorescent macroscopic lipid domains (Adapted from [2])

The two phases are displayed in different colors (the liquid disordered phase in red, the liquid ordered phase in green), making the lateral separation into domains visible. L_o and L_d domains in the micrometer range form lamellar lattices showing distinct Bragg peaks in scattering experiments. The challenges in the analysis of smaller domains (in the nanometer range) are overlapping Bragg reflections of L_o and L_d phase as well as a small number of solid orders [12]. A fluorescent microscopic image of nanoscopic domains is shown in Figure 1.22.
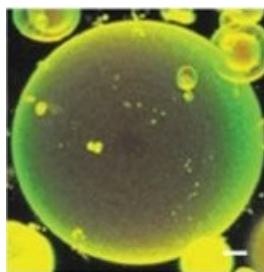
Figure 1.22: Fluorescent nanoscopic lipid domains (Adapted from [2])

The lateral separation is not visible here, because the domains are too small and supposedly not aligned enough in the different bilayers of multilamellar vesicles to be resolved. Figure 1.23 illustrates this hypothesis.
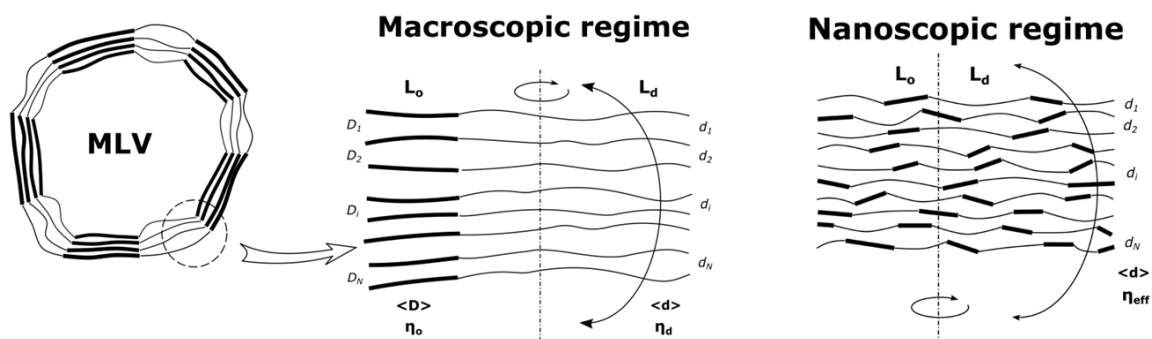
Figure 1.23: Drawing of the alignment of domains in different bilayers of multilamellar vesicles for macroscopic and nanoscopic domains

The macroscopic domains in Figure 1.23 are aligned in the different bilayers of the multilamellar vesicles, allowing to distinguish between the phases in scattering experiments. The nanoscopic domains are more randomly distributed, which is preventing a clear lateral discrimination of the phases over all bilayers. The d-spacings as well as the fluctuations, η can not be stated separately for the phases but are averaged over the bilayer.

The size of the domains is estimated to be in the range of a few nanometers up to several micrometers. Lateral membrane inhomogeneities can be randomly (ideal) or non-randomly mixed (compositional fluctuations). Domain stability and size depend on the line tension γ, which defines the free energy of the domain boundaries. Unstable domains have a line tension of about $\gamma = 0$. Stable domains can be subdivided into macroscopic, also called type II domains ($1 - 10 \ \mu m$) (see Figure 1.21) occurring for small γ and nanoscopic, or type I domains ($2 - 10 \ nm$) [10] (see Figure 1.22) with larger values for γ [21]. The line tension is mainly caused by the mismatch in bilayer thickness of the L_o and L_d phases [8]. An increased cholesterol concentration reduces the thickness mismatch, which decreases the line tension and leads to faster temperature-induced melting of the L_o domains [12]. A changing bilayer thickness that comes along with changes in the degree of lipid chain unsaturation, is restricted to the disordered phase [8].

While it is comparatively easy to monitor macroscopic domains (for example with optical techniques), nanoscopic domains are still difficult to investigate, as the structures are smaller than the optical resolution limit and therefore not directly observable. Possible methods that are currently used for investigating these structures are SAXS (Small Angle X-ray Scattering), SANS (Small Angle Neutron Scattering), FRET (Förster resonance energy transfer measurements), which is sensitive to domains larger than 2-8nm [9]. and EPR (electron paramagnetic resonance) [14].

There are also alternative interpretations to explain nano domains, such as treating them as critical fluctuations or microemulsions [10].

It was recently shown that the size of the domains in a mixture of a high-melting lipid, a low-melting lipid and cholesterol, can be controlled by the low-melting lipid. Using different ratios of the two low-melting lipids DOPC and POPC, an increase of the domain size with ascending DOPC percentage ρ_{DOPC} was established [8].

$$\rho_{DOPC} = \frac{\chi_{DOPC}}{\chi_{DOPC} + \chi_{POPC}} \; [\%] \tag{1.6}$$

An illustration about the relation between the DOPC/POPC ratio and the size of the domains is given in Figure 1.24.
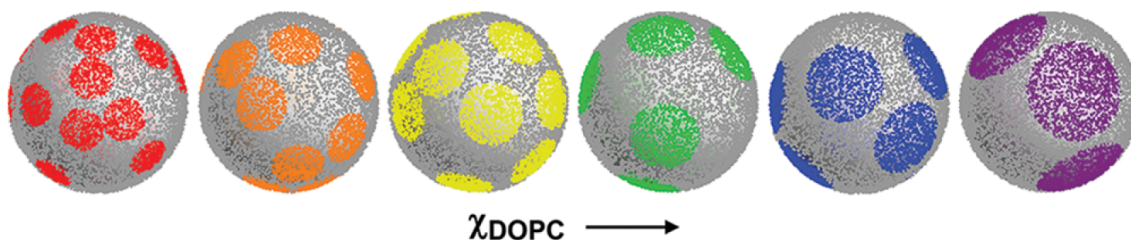
Figure 1.24: Different sizes of lipid domains (Adapted from [8])

The figure is a product of Monte Carlo (MC) simulations that were used to analyze SANS data from the group of J. Katsaras [8]. It shows the growth of the domains depending on the DOPC amount in the sample.

The transition from nano to macro domains depending on the DOPC/POPC ratio can also be comprehended with the help of phase diagrams in Figure 1.25.
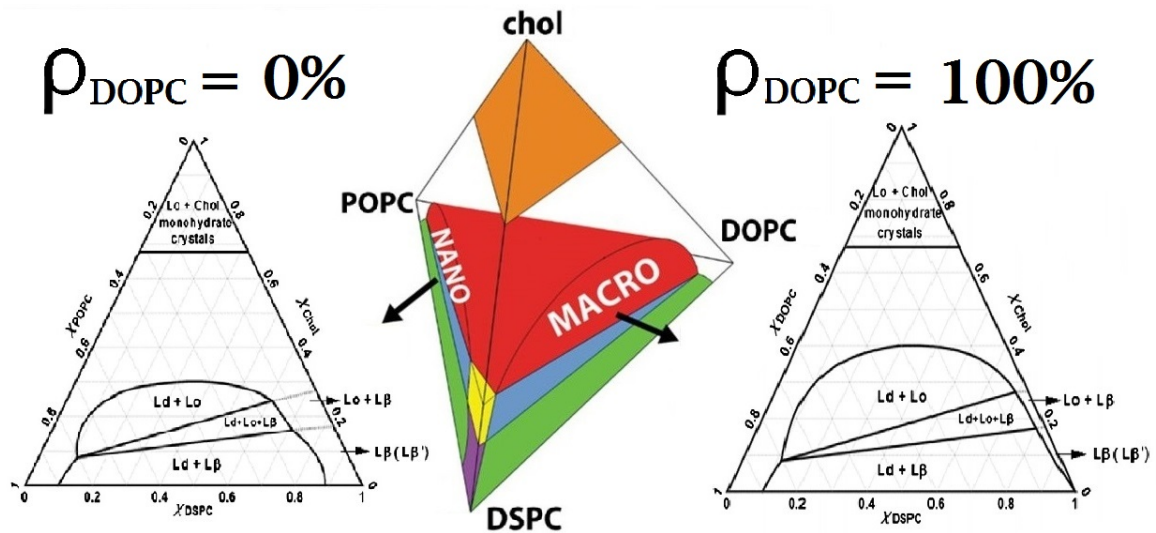
Figure 1.25: Compositional phase diagrams of DSPC/POPC/Cholesterol (left), DSPC/DOPC/POPC/Cholesterol (middle) and DSPC/DOPC/Cholesterol (right) (Adapted from [2] and [16])

The phase diagram on the left side of Figure 1.25 transforms into the one on the right side by increasing the ratio of DOPC/POPC in the sample. For phase diagrams of low DOPC content the coexisting phase region consists of nano domains, whereas for high DOPC contents macro domains are built.

Membrane **rafts** are functional, compositionally distinct domains in mammalian plasma membranes. They are thought to be small, highly dynamic platforms containing sphingolipids and/or cholesterol [12], [21], suspected to be important for signaling, membrane transport, and protein sorting among others [9]. The raft model was introduced by Simons and Ikonen 1997 [35], however direct evidence for their existence has been elusive so far.

1.6 Synchrotrons

A synchrotron is an accelerator in which charged particles are forced on a circular path and accelerated to very high energies via electromagnetic fields. For achieving such high velocities the path has to be under ultra high vacuum (UHV) to avoid collisions of the particles with gas molecules. The particles are initially injected into the synchrotron with a high velocity from a pre-accelerator. Figure 1.26 shows the schematic layout of a synchrotron.
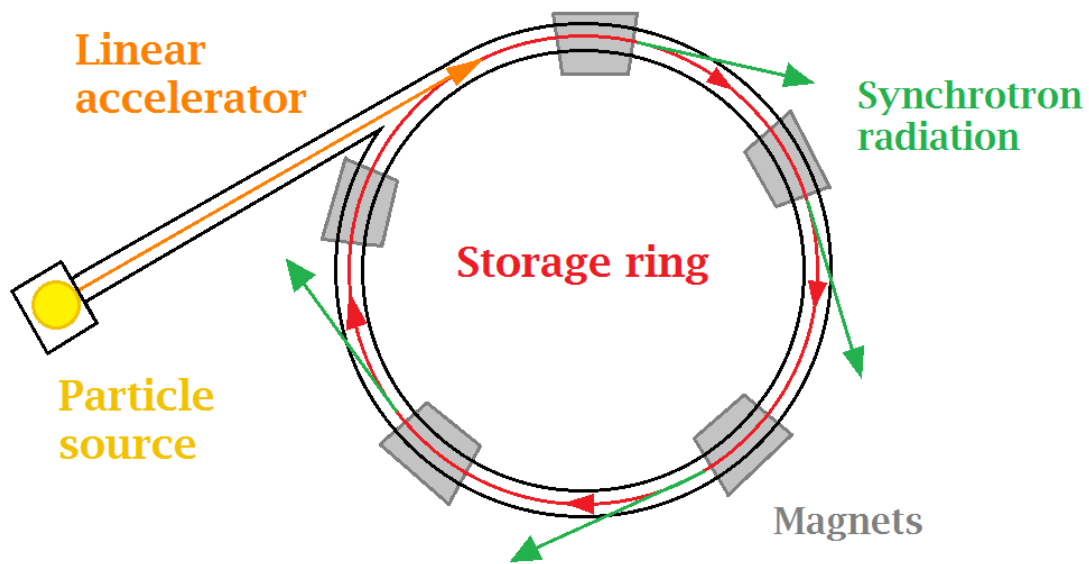
Figure 1.26: Simplified layout of a synchrotron

Charged, accelerated particles can send out so called synchrotron radiation. This special kind of radiation is a form of bremsstrahlung that arises when particles with velocities close to the speed of light are forced on a curved path, which is a form of acceleration. It refers to electromagnetic radiation that is occurring tangential to the direction of moving, highly energetic particles (green arrows in Figure 1.26).

As a result of this radiation, the particles lose a lot of energy every cycle. Equation 1.7 gives the relation for the energy loss ΔE depending on the atomic number Z, the elementary charge e, β which is the relation between the particle velocity v and the speed of light c ($\beta = \frac{v}{c}$), γ the Lorentz factor $\left(\gamma = \frac{1}{\sqrt{1-\beta^2}}\right)$, the vacuum permittivity ϵ_0 and the radius of the storage ring R.

$$\Delta E = \frac{(Ze^2) \cdot \beta^2 \cdot \gamma^4}{\epsilon_0 \cdot 3R} \tag{1.7}$$

The radiation causing this huge energy loss for high velocities is not a waste-product though. It can be used for a manifold of applications because of its extraordinary properties. These are, for example, the broad spectrum of the radiation, that reaches continuously from the infrared to the (hard) X-ray range with a high radiant intensity, high flux and high brilliance. Synchrotron radiation is very stable, linear and circular polarized, and has a pulsed structure. The very short pulses allow for measurements on the time scale of the pulse.

Synchrotron radiation does not only occur when it is artificially generated in accelerators, it also arises naturally. It always appears when a hot plasma is located in a magnetic field. Cosmic synchrotron sources are pulsars, radio galaxies and quasars for instance. Another example is Jupiter, that makes high energetic electrons radiate by forcing them into a spiral path in its orbit with very strong magnetic fields [32]. There are several synchrotrons all over the world; located in Europe are for example the ESRF (European Synchrotron Radiation Facility) in Grenoble (France) or the MAX IV Laboratory in Lund (Sweden). However the two synchrotrons that were important for this work were Elettra in Trieste (Italy) and DESY in Hamburg (Germany). They are described in 1.6.1 and 1.6.2.

1.6.1 Elettra, Trieste (Italy)

Elettra Sincrotrone Trieste in Basovizza, Italy is an international research center that was established in 1993. It has been developed further in the last few years and now contains two light sources - a third generation storage ring (Elettra) and a free electron laser (SR-FEL). Figure 1.27 shows models of the synchrotron as they can be seen inside its experimental hall.

Figure 1.27: Models of the Elettra Sincrotrone Trieste

The storage ring has a circumference of roughly 260 m and is operated in top-up operating mode. This means that the current in the storage ring is kept constant, which is accomplished via frequent injections of particles. The energy range of the storage ring goes from 0,75 up to 2,5 GeV, usually it is operated at 2,4 GeV. The energy loss per turn for the maximum energy of 2.5 GeV is about 388 keV.

The magnetic system of the storage ring consists of different parts. There are bending magnets for deflecting the electron beam into the circular path, quadrupoles to focus the beam, sextupoles to compensate non-linear and chromatic effects and steerer magnets for making small adjustments to the trajectory. The magnets are arranged

in a lattice of the expanded Chaseman Green type, also called double bend achromat. The ring is built of 12 identical magnet groupings of this type.

The wavelength of the light can either be tuned by varying the electromagnetic field, which can be regulated by modifying the current in the coils, or by adjusting the permanent magnets, where the field can be changed by varying the distance between the magnet arrays.

Photons in the energy range from a few to several tens of keV with a spectral brightness of up to 1019 Jkg^{-1} are generated.

Elettra contains several beamlines for different techniques like photoelectron emission, imaging, scattering, reflection/emission, absorption, diffraction and lithography. The measurements for this thesis were taken at the Austrian SAXS beamline at Elettra. For details about small angle scattering see 2.3. Information about the Elettra synchrotron was taken from their website.[2]

1.6.2 DESY, Hamburg (Germany)

The German Electron Synchrotron (Deutsches Elektronen Synchrotron - DESY) is a research center mainly located in Hamburg, Germany, which was established in 1959. It develops and operates on particle accelerators and enables research on particle physics and photon science. The center incorporates different storage rings and free electron lasers.

There are three main accelerators dedicated to the generation of photons: The first one is PETRA III (Positron-Electron Tandem Ring Accelerator), a 3rd generation synchrotron radiation source of 2,3 km circumference and thereby the biggest and most brilliant storage ring X-ray source worldwide. In one of it's precursors (PE-

---

[2]www.elettra.trieste.it

TRA) the existence of gluons was proven. PETRA is now used as a pre-accelerator for HERA (Hadron-Electron Ring Accelerator) in which fundamental research via particle collisions is performed. The second one is FLASH (Free Electron LASer Hamburg), which provides ultra short flashes of soft X-ray light, and thirdly the European XFEL (X-ray Free Electron Laser), which is currently being built and which is announced to produce the world's most intensive X-ray flash. Figure 1.28 gives an overview over the X-ray sources via aerial photographs.[3]

Figure 1.28: Overview over Petra III, Flash and XFEL (left) and picture of the experimental hall of PETRA III (right)[3]

PETRA III is run in top-up mode and provides a particle energy of 6 GeV, a beam current of 100 mA and a photon flux in the energy range of 50-150 keV. It is composed of different magnets: dipoles, quadrupoles, sextupoles, damping wigglers and undulators. Measurements for this thesis were taken at the P12 EMBL BioSAXS Beamline at PETRA III, where low scattering background and energy tunability for SAXS experiments are provided.

---

[3]Details and pictures about DESY were taken from 'www.desy.de', 'www.lightsources.org' and 'photon-science.desy.de'.

Chapter 2

Methods

2.1 Phosphate assay

In a phosphate assay the organic groups of the lipids are cleaved off by chemical means to measure the remaining PO_4 groups and thereby determining the content of phospholipid in a stock solution with a spectrophotometer. The procedure is described on the following pages.

Firstly, the required equipment has to be cleaned carefully as the measurement is sensitive and even small quantities of contamination could have an effect on the results. For this purpose 3 different cleaning agents are used: MQ (Milli-Q - purified water), $MeOH$ and $CHCl_3$. The water dissolves ions and polar molecules, $MeOH$ does the same but additionally to that it removes the residual water so that it does not generate an emulsion with the $CHCl_3$ which dissolves organic molecules.

The phosphate standard is prepared from a primary phosphorous standard (>99,99% pure J.T.Baker KH_2PO_4, ULTREX ultrapure reagent from Sigma Aldrich, product number 229806). 350 mg of it are weighed out and incubated until the weight stops decreasing from leaving water. Then the powder is transferred to a 500 mL volumetric flask and dissolved to a target concentration of 5 mM.

The (thawed and vortexed) lipid stock solution is taken up into a (clean) syringe and precisely adjusted portions of it are distributed into 13x100 mm culture tubes with

a Hamilton Repeating Dispenser. (The amount of stock dispensed depends on the supposed lipid concentration in the stock solution in order to be in the middle of the calibration curve.)

Next, the standard inorganic phosphate solution is dispensed into individual culture tubes. Thereby different amounts of phosphate standards are filled into each tube (usually between 0 and 50 nmol) so that a large range of concentrations is covered.

10% sulfuric acid is added to each tube to cleave the bonds and thereby remove the hydrocarbons from the phosphate in a process called 'ashing'. The tubes are randomly distributed on a heating plate so that possible unbalanced heating does not have a linear effect on the ashing process. This transaction is carried out at $200°C$ for 2 hours. After the first hour 30% H_2O_2 (phosphate free) is added to the tubes to oxidize organic matter, then the incubation is continued for one more hour on the heating block to decompose the H_2O_2.

After 2 hours the tubes have to be checked for being colorless. If color persists, it means that there are organic residues in the sample that are not oxidized. In that case the same amount of H_2O_2 has to be added to all the tubes again and they have to stay heated for 40 more minutes. If the tubes are all clear and colorless they can be cooled down. At this point all the phosphate groups should have been freed from the rest of the phospholipid.

During the last hour of ashing the coloring reagent is prepared by mixing water and ascorbic acid (vitamine C). The third component is (5%) ammonium molybdate but it is only added just before the color reagent is used because it slowly starts breaking down in the mixture.

Once the tubes have cooled to room temperature, water is added to wash down potential phosphate on the sides of the tubes, then color reagent is added without wetting

the sides of the tubes. The phosphate-coloring reagent solution is then incubated for 20 minutes in the water bath at $45°C$, for facilitating the reaction of the phosphates with the color reagent.

At that point the preparation is finished and the samples can be measured in the spectrophotometer.

Thereby after carefully cleaning the cuvette, the standards are measured first and afterwards the samples. The cuvette is always filled twice - the first filling is just for cleaning purposes, it is removed without being measured.

The spectrophotometer detects the transmission of light that is sent through the samples. Based on the transmission, the absorbance (A_λ) is calculated from the ratio of the intensity of the incident light (I_0) and the intensity of the transmitted light (I_1) via the Beer-Lambert law (Eq.2.1).

$$A_\lambda = log\left(\frac{I_0}{I_1}\right) = \epsilon_\lambda \cdot c \cdot d \tag{2.1}$$

The equation also links the absorbance to the molar attenuation coefficient (ϵ_λ), the molar concentration of the absorbing substance (c) and the thickness of the radiographed body (d).

The standards are used to generate a calibration curve that shows how the absorbance is related to the content of phosphate. Knowing the volumes of the samples, the lipid concentrations in the stocks can be calculated from the absolute number of moles of phosphate in the sample.

2.2 Sample preparation

Samples were prepared as outlined by previously established protocols [8] and were consistent for all measurements. The 4-component lipid mixtures were all midpoint samples with tielines similar to the ones in Figure 2.1. The DOPC/POPC ratio was increased following the arrow in the figure below.
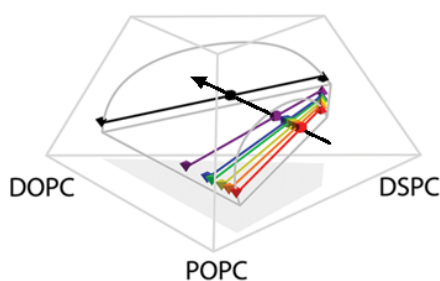
Figure 2.1: Compositional phase diagram of DSPC/DOPC/POPC/Cholesterol (Adapted from [8])

1,2-Distearoyl-sn-glycero-3-phosphocholine (DSPC), 1,2-Dioleoyl-sn-glycero-3-phos-phocholine (DOPC) and 1-Palmitoyl-2-oleoyl-sn-glycero-3-phosphorylcholine (POPC) were purchased from Avanti Polar Lipids, Cholesterol from Sigma Aldrich and were used as received.

Firstly, predefined amounts of lipid in powder form were weighed into separate glass vials. Then the appropriate amounts of a 2:1 chloroform-methanol mixture were added so that stock solutions of about 20 mg lipid per mL solution were produced. An inorganic phosphate assay was then performed (see section 2.1) to determine the stock concentration within 2% as all phospholipids hold a varying amount of water. 17 quarternary mixtures of DSPC, DOPC, POPC and cholesterol with different compositions were prepared following the tieline at constant DSPC (0,39 mol) and choles-

terol (0,22 mol) content in a phase diagram at 20°C. Desired amounts of the lipid stock solutions were transferred into 17 new glass vials to achieve the compositions shown in Table 2.1 - with ρ_{DOPC} the ratio of DOPC to POPC in the sample (see Equation 1.6).

Table 2.1: Overview over the prepared sample compositions

	ρ_{DOPC} [%]	DSPC [mol]	DOPC [mol]	POPC [mol]	Cholesterol [mol]
A1	0	0,39	0,00	0,39	0,22
A2	5	0,39	0,02	0,37	0,22
A3	10	0,39	0,04	0,35	0,22
A4	15	0,39	0,06	0,33	0,22
A5	20	0,39	0,08	0,31	0,22
A6	25	0,39	0,10	0,29	0,22
A7	30	0,39	0,12	0,27	0,22
A8	35	0,39	0,14	0,25	0,22
A9	40	0,39	0,16	0,23	0,22
A10	45	0,39	0,18	0,21	0,22
A11	50	0,39	0,20	0,20	0,22
A12	60	0,39	0,23	0,16	0,22
A13	65	0,39	0,25	0,14	0,22
A14	70	0,39	0,27	0,12	0,22
A15	80	0,39	0,31	0,08	0,22
A16	90	0,39	0,35	0,04	0,22
A17	100	0,39	0,39	0,00	0,22

The completed mixtures were then put under a nitrogen stream and evaporated for about 30 minutes, producing lipid films on the bottom of the vials. Subsequently, they were put under vacuum over night to remove the remaining solvent.

The samples were hydrated with 200 μL of H_2O and sealed under an argon atmosphere to prevent sample oxidation.

The samples then underwent six **'freeze and thaw' cycles** to break the existing lipid bilayers of the vesicles and make the lipids form well mixed multilamellar vesicles. These cycles consisted of four parts:

- Incubating the samples in an oven at 55°C for 30 minutes

- Shaking them for 5 minutes (also at 55°C)

- Freezing the samples by means of liquid nitrogen for a few seconds

- Shaking them again at 55°C with a vortexer, this time for 15 minutes

Afterwards the samples were stored in a freezer at -80°C and just heated up to 55°C once again shortly before the measurements.

2.3   Small angle X-ray scattering (SAXS)

X-ray radiation is a part of the electromagnetic spectrum originating either from the acceleration of highly energetic electrons (bremsstrahlung) or from certain transitions of electrons between the shells within atoms (characteristic X-ray radiation). The wavelength of X-rays lies below 0.3 nm [33].

Small angle X-ray scattering (SAXS) is an accurate, basically non-destructive method that uses elastic scattering of X-ray radiation at low angles (typically 0.1-10°) to gain structural information in the nanometer range, which makes it ideal for the study of mesoscopic structures. It is sensitive to inhomogeneities in the electron density, because the scattered X-rays interact with the electrons of the atoms in the sample. SAXS can be used to measure the averaged particle size and shapes among other parameters. The resolution of SAXS measurements is typically in the range of 1-100 nm [33]. An advantage of SAXS is, that relatively small quantities of samples are needed; however a risk is radiation damage of the sample, playing a role at long measuring times or highly intense beams as provided at synchrotron beamlines.

In SAXS, X-ray tubes or synchrotrons are used as X-ray sources. A highly collimated beam is sent through the sample (transmission mode) and the scattered beam containing signals from every particle it interacted with, is detected on the other side. For shaping the beam there are two different possibilities, point-collimation and line-collimation, whereby the first was used for the measurements in this thesis. For measuring surface near particles selectively, the so called reflection mode can be operated, which is a variation of SAXS called GI-SAXS (grazing incidence SAXS), but it was not used for this work. The setup of a typical SAXS machine can be seen in Figure 2.2.
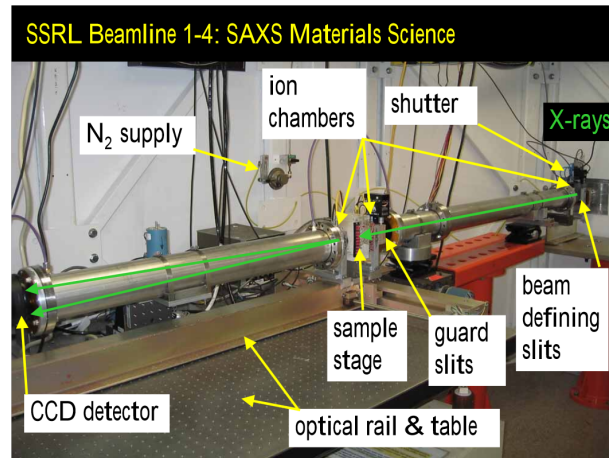
Figure 2.2: Set-up of a SAXS machine (Adapted from [27])

The beam comes from the X-ray source, is defined by slits, goes into the ion chambers for radiation detection, through the sample and then to the detector, which is relatively far away from the sample for the SAXS alignment, when compared to wide angle X-ray scattering (WAXS) for instance. After the detection, the scattering pattern has to be reconstructed in a mathematical way, which accounts for detector distance, detector geometry and the beam profile. As the phases of the detected waves are lost, no 3-dimensional representation is possible [33]. A description of the scattering in the SAXS setup is given in Figure 2.3. [1]
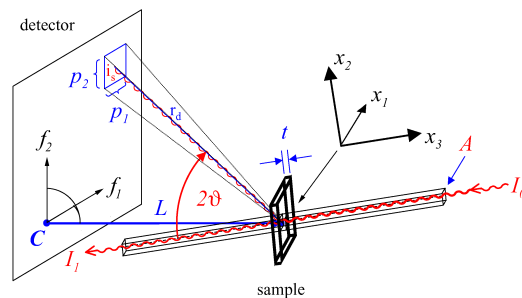
Figure 2.3: Scattering geometry in SAXS [1]

---

[1]Figure resumed from 'www.esrf.eu'

The incident X-ray beam I_0 impacts the sample and is partly scattered, which leads to a scattering angle of 2θ between the non-diverted part I_1 and the scattered X-rays I_S. On the detector, the scattered content is collected and the impact angle of the impinging X-rays is measured.

The relation between the energy (E) and the wavelength (λ) is given by the DeBroglie equation (Eq.2.2) where h is Planck's constant and c is the speed of light.

$$E = \frac{hc}{\lambda} \tag{2.2}$$

The equation shows, that the smaller wavelengths are wanted, for being able to examine tiny structures for instance, the higher the energies get. The two different ways X-rays can interact with matter are absorption and scattering. When waves are scattered, interference patterns occur. The optical path for 2 overlaid waves is shown in Figure 2.4.
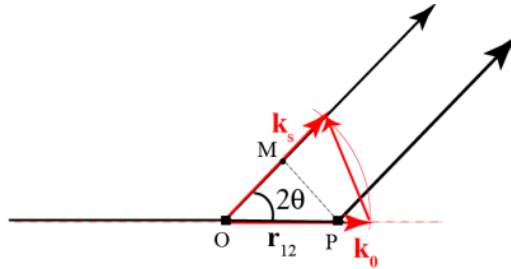
Figure 2.4: Interference of two waves (Adapted from [31])

$\vec{k_0}$ and $\vec{k_S}$ are the wave vectors of the incident respectively the scattered wave $(k = \frac{2\pi}{\lambda})$. The amplitude of the two interfering waves is given by the phase difference ϕ (Eq.2.3), depending on the path difference $\vec{r_{12}}$ [31].

$$\Delta\phi = \frac{2\pi}{\lambda}(\vec{r_{12}} \cdot \vec{k_0} - \vec{r_{12}} \cdot \vec{k_s}) = \vec{r_{12}} \cdot \vec{q} \cdot sin(\theta) \tag{2.3}$$

On the right side of Equation 2.3 the relation to the scattering vector $\vec{q}$, also called momentum transfer, and the scattering angle θ are shown. Bragg's Law gives the condition for constructive interference (Equation 2.4) where d is the lamellar repeat distance and n is an integer value of the diffraction order.

$$n \cdot \lambda = 2d \cdot sin(\theta) \tag{2.4}$$

Referring to Bragg's Law, larger structures implicate smaller scattering angles if the wavelength is constant. The relation between the repeat distance of the bilayers and q can be depicted in the following way (Eq.2.5).

$$d = \frac{2\pi}{q} \tag{2.5}$$

Consequently, the scattering vector for the first order can be represented as it is shown in Eq.2.6 [33].

$$q = \frac{4\pi}{\lambda} \cdot sin(\theta) \tag{2.6}$$

The scattering vector is a very important parameter in small angle scattering, as it is directly measured and it allows for the easy calculation of the bilayer thickness (Eq.2.5). Most oftenly, SAXS data are shown as their scattered intensities depending on q. In this way experiments at different energies can be compared as the data are not depending on the wavelength.

2.4 Differential Scanning Calorimetry (DSC)

DSC is a common method used for analysing thermal events, especially phase transitions. The difference in the heat capacities of a sample and a reference (c_P) is obtained from the difference in the measured heat flows that are required for heating at a constant rate. Sample and reference are heated in such a way that the temperatures remain the same. The heat capacity difference, depending on the temperature, shows a peak if the sample underwent a first order phase transition. This method is useful for identifying substances by their thermal behavior, generating phase diagrams and determining thermodynamic parameters such as the total transition enthalpy (Δh_{cal}), the van't Hoff enthalpy (ΔH_{vH}), the entropy or the transition temperatures. The parameters can be directly or indirectly extracted from the thermogram.

As an example, a thermogram of DPPC is shown in Figure 2.5, which highlights the pre-transition (36°C), where periodic ripples are formed in the membrane [30], and the main transition (41°C) from gel to fluid phase.
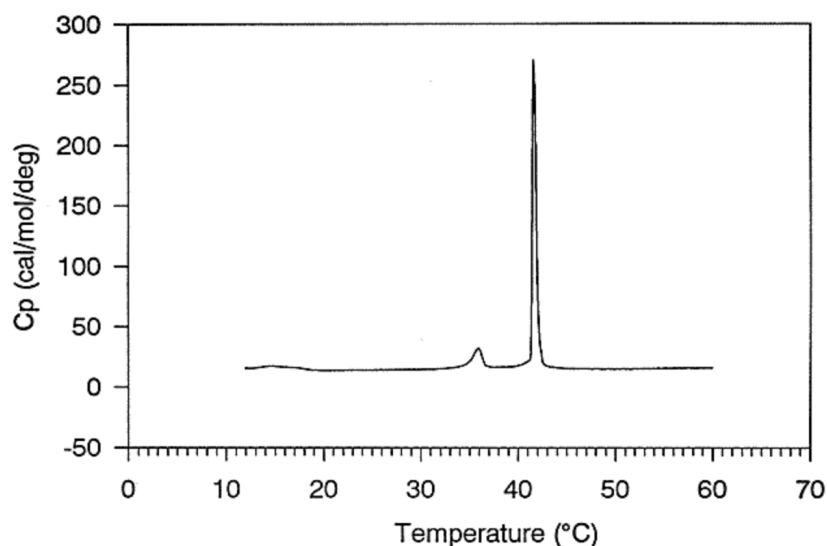
Figure 2.5: DSC profile of a DPPC sample (Adapted from [15])

Chapter 3

Measurements and results

The measurements can be split up into two parts. The first one (described in section 3.1) is the collection of data at fixed compositions but different temperatures to find the melting temperatures of the L_o domains. In the second part (described in section 3.2) different compositions at a constant temperature of 20°C are examined to investigate the dependence of the domain size on the DOPC/POPC ratio ρ_{DOPC}.

3.1 Temperature measurements

3.1.1 SAXS measurements at different temperatures

Temperature series measurements were taken at the Elettra Sincrotrone Trieste. The samples were slowly heated, starting from a temperature of 20°C up to a maximum temperature of 60°C, with a heating rate of 1°C per minute, to observe the structural changes of the lipid bilayer depending on the temperature.

The sample shown in Figure 3.1 was collected at 20°C. It exhibits macro domains that can be identified by Bragg peaks corresponding to two different d-spacings. Figure 3.2 shows the same sample at 60°C, for which only single peaks can be observed. This coalescence of Bragg peaks indicates that the liquid ordered domains melted during the heating process and the sample has passed from the phase separated domain structure into a pure liquid disordered phase.
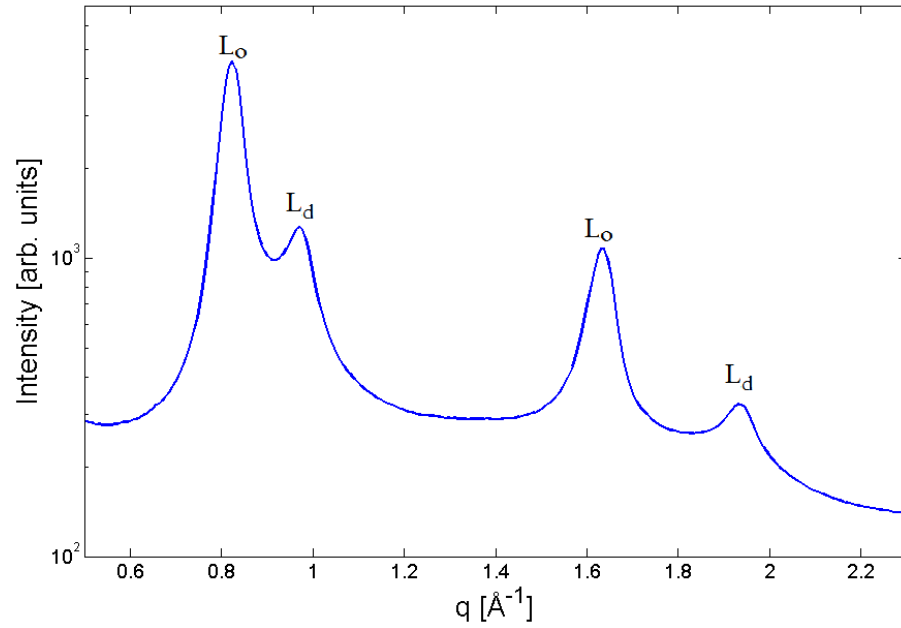
Figure 3.1: DSPC/DOPC/POPC/Cholesterol mixture A12 (ρ_{DOPC}=60%) at 20°C
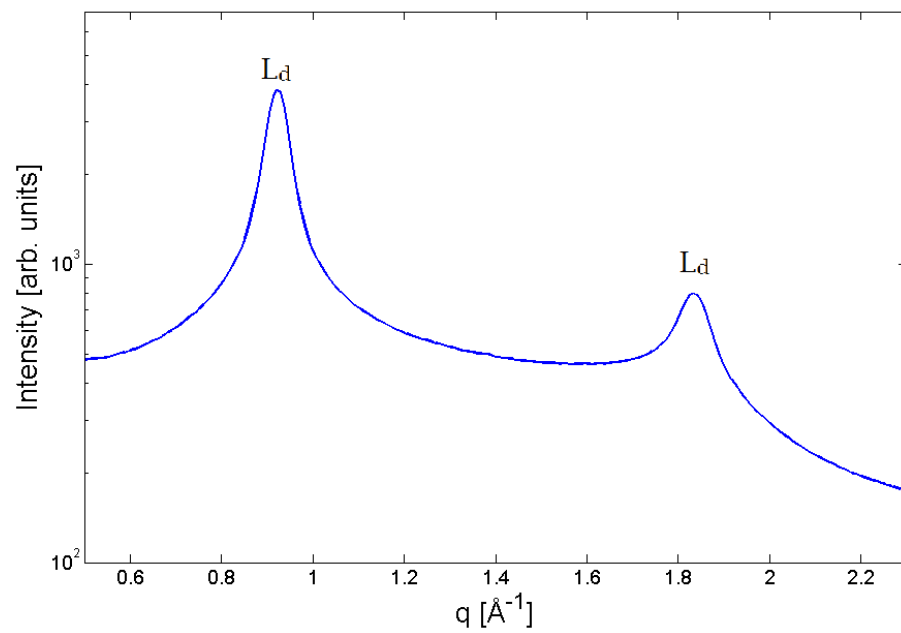
Figure 3.2: DSPC/DOPC/POPC/Cholesterol mixture A12 (ρ_{DOPC}=60%) at 60°C

The goal of the study was to examine the temperature dependent transition into the pure L_d phase for different compositions. A sketch of a phase diagram where the phase depends on the composition and the temperature can be found in Figure 1.19 in section 1.4. The example shown in Figure 3.3 gives an overview of different measured temperatures. The transition temperature, where the two second order peaks merge into one, appears to be at about 41°C for a ratio of $\rho_{DOPC} = 65\%$.
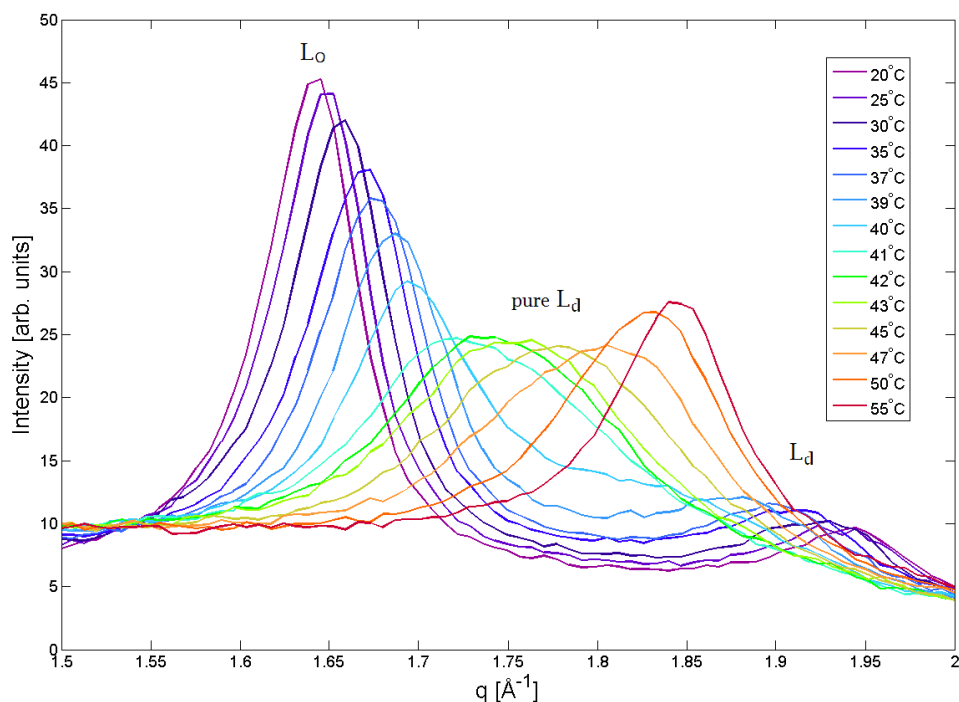
Figure 3.3: Second order peak(s) of SAXS measurements at different selected temperatures for the DSPC/DOPC/POPC/Cholesterol sample A13 ($\rho_{DOPC} = 65\%$)

The sample was heated in 1°C steps between 20 and 60°C without additional equilibration times. This fast heating process might have slightly shifted the transition temperature to a higher value.

The transition temperatures of the measured macro domain samples are shown in Table 3.1.

Table 3.1: Transition temperatures of different DSPC/DOPC/POPC/Cholesterol compositions

	ρ_{DOPC} [%]	DSPC	DOPC	POPC	Cholesterol	T_{trans} [°C]
A9	40	0,39	0,16	0,23	0,22	35
A12	60	0,39	0,23	0,16	0,22	below 40
A13	65	0,39	0,25	0,14	0,22	41
A14	70	0,39	0,27	0,12	0,22	40

The measurements for the samples in Table 3.1 were collected as follows:

For A9 and A13 a fine scan was made, where the temperature was evenly increased and measured in 1°C steps without equilibration. For A12 and A14 the temperature was increased in 5°C steps from 20 to 40°C and in 2°C steps between 40 and 56°C with a final measurement at 60°C, the temperature was held constant for 10 minutes at every step before the measurements were taken.

For this reason the actual values for the transition temperatures in A9 and A13 may be lower than the values shown in the table above. The transition temperature for A12 lies between 35 and 40°C, the form of the curves at lower temperatures suggests a transition closer to 40°C. For A14 the transition seems to take place at about 40°C. In summary it can be concluded that the transition temperature is shifted to higher values if the relative amount of DOPC in the sample compared to POPC is increased. For more detailed information about the transition temperatures DSC (Differential Scanning Calorimetry) measurements were made (see sec. 3.1.2).

During the heating process the d-spacing, which is the distance between the beginning of two different bilayers (see Figure 1.16), changes depending on the temperature. This relation is shown in Figure 3.4.
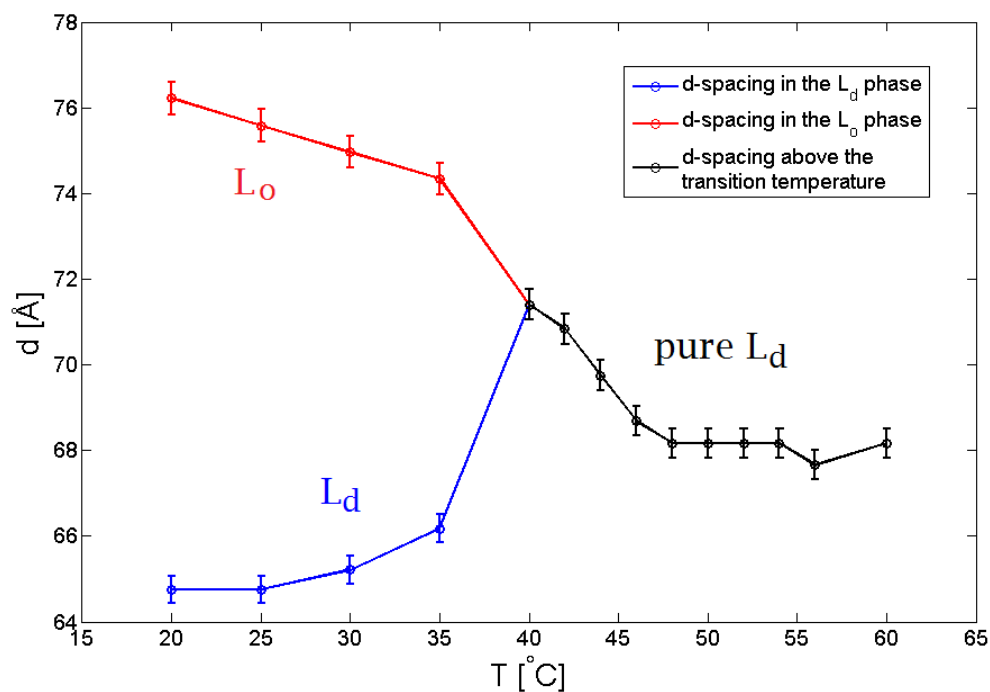
Figure 3.4: d-spacing depending on the temperature for A12 ($\rho_{DOPC} = 60\%$)

Figure 3.4 demonstrates how the different d-spacings of the L_o and the L_d phase converge until they merge at the transition temperature of 40°C. At higher temperatures the d-spacing decreases from above 71 Å at 40°C to about 68 Å at 48°C, then it remains constant up to 60°C.

In the low temperature range, where the phases are coexisting, the L_o phase is between 8 and 11 Å thicker than the L_d phase because of its more ordered structure due to the higher cholesterol content. When domains melt into a pure liquid disordered phase, the d-spacing of the pure L_d phase lies between the ones of the coexisting phases, decreasing with increasing temperature.

The Ising model is a common model for critical behavior. In this case the height mismatch of the d-spacings of the two phases Δd was used as the order parameter, as L_o and L_d phase are laterally separated below a critical temperature and melt into a homogeneous L_d phase above T_C. Equation 3.1 was used to describe the relation between height mismatch and temperature.

$$\Delta d \propto (T_C - T)^\beta \tag{3.1}$$

β is the critical parameter, suggesting a 2D Ising model for $\beta = 0{,}125$ and a 3D Ising model for $\beta = 0{,}325$ (compare [10]).

The comparison of the scattering data of A13 ($\rho_{DOPC} = 65\%$, $T_C = 41°C$) with Equation 3.1 (which is the exact function fit) shows a better compliance with the 2D Ising model, as shown in Figure 3.5.
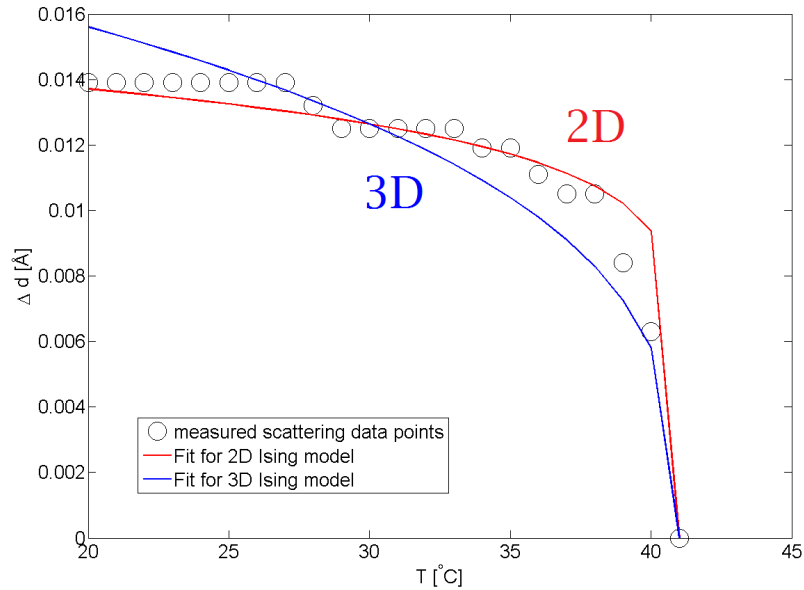
Figure 3.5: Scattering data of A13 ($\rho_{DOPC} = 65\%$) compared to a 2D Ising model (red) and a 3D Ising model (blue)

To evaluate the extent of radiation damage during longer exposure times, a measurement of about 5 hours at a constant temperature of 20°C was recorded, where the sample was radiated for several minutes every 10 minutes. The comparison between before and after the exposure is shown in Figure 3.6.
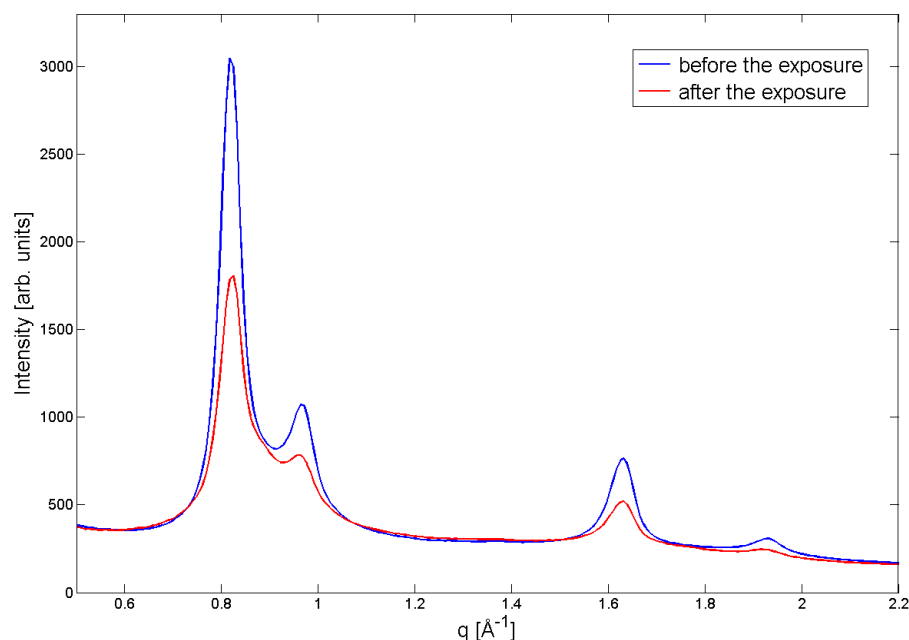
Figure 3.6: Comparison of SAXS scattering curves of a DSPC/DOPC/POPC/Cholesterol mixture before (blue) and after (red) its exposure to radiation

The radiation does not seem to change the structure of the domains as the two Bragg peaks caused by the macro domains are still present after the exposure. Although, radiation does decrease the measured intensity, because more and more lipid vesicles are broken apart due to radiolysis. The scattering signal is proportional to the amount of sample exposed, thus scattered intensity decreases with sample breakdown.

3.1.2 Differential Scanning Calorimetry measurements

DSC was utilized to get more information about the transition temperatures, where the domain structure passes into a homogeneous liquid disordered phase, for different sample compositions. These measurements made it possible to observe the transitions for nano domains, which could not be resolved by small angle x-ray scattering (see sec. 3.1.1).

The samples were heated up from 10 to 60°C with a heating rate of 30°C per hour and then cooled down to 10°C with a cooling rate of 30°C per hour. Milli-Q water was prepared and used as reference. Figures 3.7 and 3.8 show the measurements of the differential heat capacity for samples containing nanoscopic (green) and macroscopic domains (red) depending on the temperature.
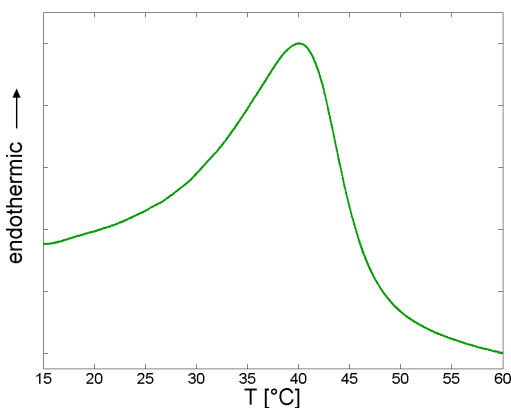
Figure 3.7: DSC profile of a sample containing nanoscopic domains ($\rho_{DOPC} = 5\%$)
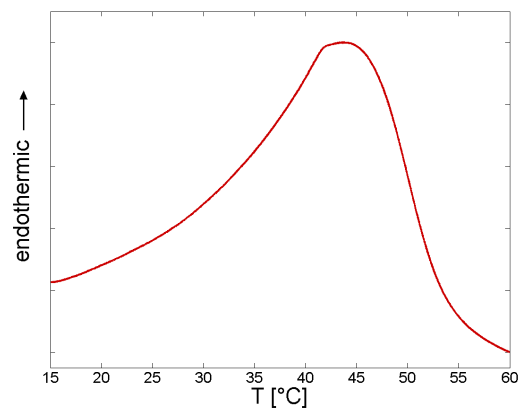
Figure 3.8: DSC profile of a sample containing macroscopic domains ($\rho_{DOPC} = 90\%$)

The transition between the domain structure and the pure L_d phase is characterized by a peak in the heat capacity. The peaks are very broad, for nanoscopic as well as for macroscopic samples, compared to the sharp peaks at the transition between gel and fluid phase for pure lipids like DPPC for example [15], indicating that the

melting transition is of low cooperativity. Nevertheless, the transition can clearly be observed, even though the transition temperatures can only be determined within certain errors. The measurements for nanoscopic domains conform well to former results collected by J. Nickels et al. [24]. However, there seems to be a small difference in the shape of the curves between nanoscopic and macroscopic domains, as they are slightly changing to less symmetric shapes with increasing ρ_{DOPC}. Figure 3.9 shows the transitions for different DOPC/POPC ratios, with $c_{P(norm)}$, the differential heat capacity normalized to values between 0 and 1.
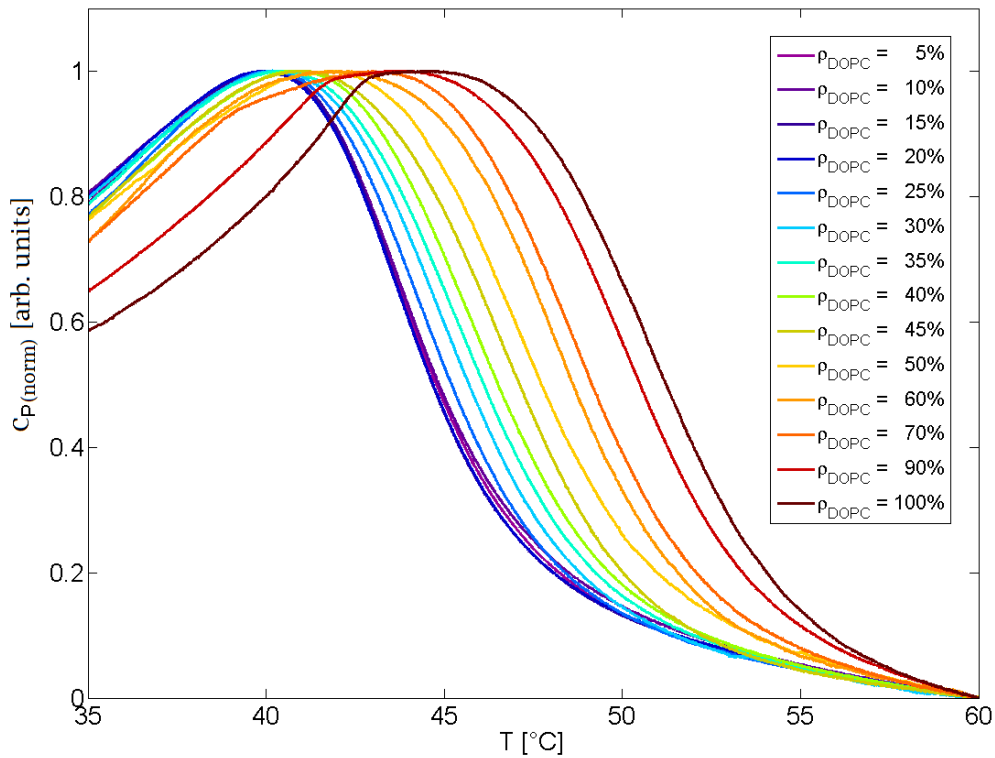
Figure 3.9: DSC profiles for different sample compositions

The melting of the nanoscopic L_o domains ($\rho_{DOPC} \leq 20\%$) appears to be independent of the composition, whereas the transitions for macroscopic L_o domains ($\rho_{DOPC} \geq 25\%$) are shifted to higher temperatures with increasing DOPC content.

The trend of the transition temperatures depending on ρ_{DOPC} is shown in Figure 3.10.
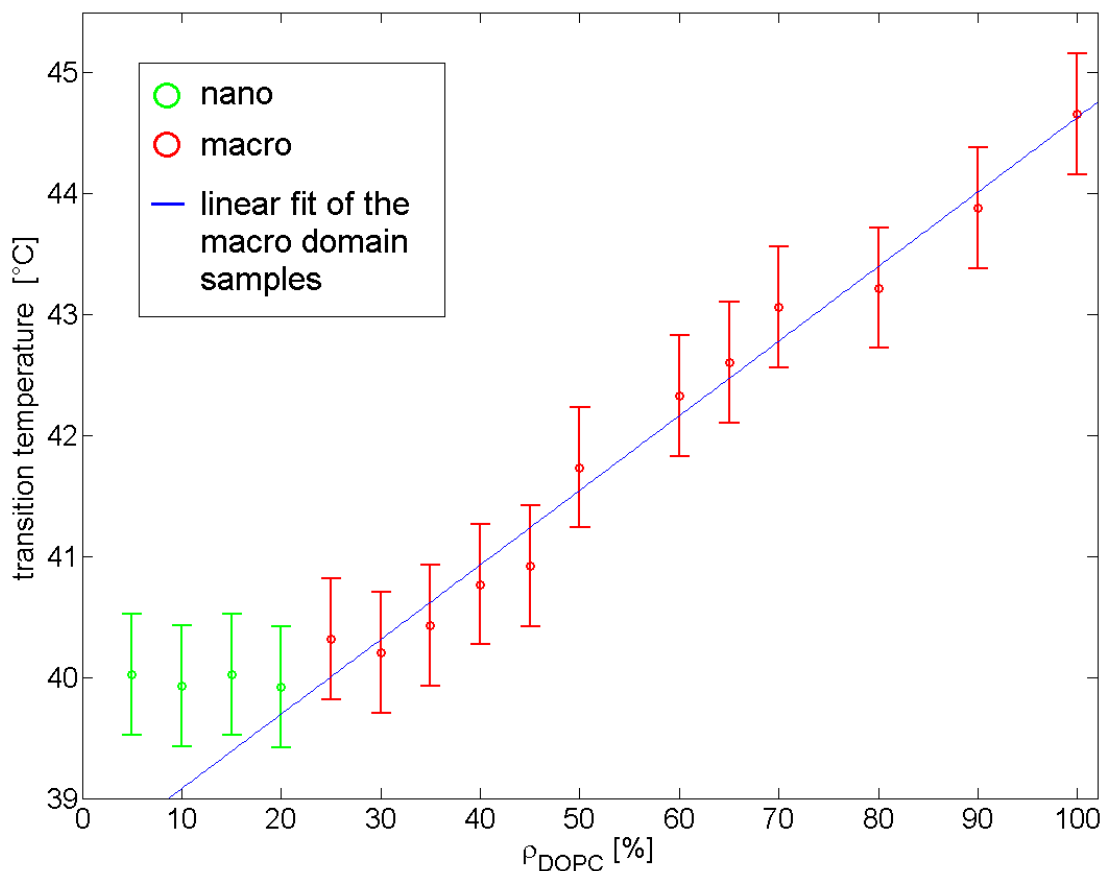
Figure 3.10: Transition temperatures depending on the DOPC/POPC ratio

The transition temperature for nanoscopic domains (green) appears to be at about 40°C, independent of the composition, whereas the melting of the macroscopic domains (red) occurs at temperatures between 40 and 45°C, depending on the DOPC content. The trend of the measured macro domain samples suggests a linear behavior, where the transition temperature rises directly proportional to ρ_{DOPC}, which is displayed with a blue line in Figure 3.10.

When comparing the values of the transition temperatures from SAXS (sec. 3.1.1) and DSC measurements, a shift of a few °C is observed. A possible explanation could be that for DSC the transition temperature is obtained from the midpoint of the peak in the differential heat capacity profile, whereas for SAXS it is the temperature above which it is no longer possible to distinguish between different d-spacings in the scattering curves, which occurs earlier in temperature because of the broadness of the melting transition.

The trend of rising transition temperatures with increasing DOPC content was observed with both measurement techniques.

3.2 Measurements at a constant temperature

The measurements in this chapter were all taken at a constant temperature of 20°C at the P12 EMBL BioSAXS Beamline at PETRA III in Hamburg. 17 samples with increasing ρ_{DOPC} were measured (for their compositions and preparation see section 2.2), where nanoscopic and macroscopic samples could be discriminated.

3.2.1 Analysis with an SDP-GAP program for MLVs

The program used for the following data modeling procedure was an SDP-GAP program for multilamellar vesicles developed by P. Heftberger [11]. It is based on the GAP program generated by G. Pabst [26]. The difference to the original program is the division of the lipids into several parts in a so called "parsing scheme" (see Figure 3.11) put forward by N. Kucerka and co-workers with the Scattering Density Profile (SDP) model [17].
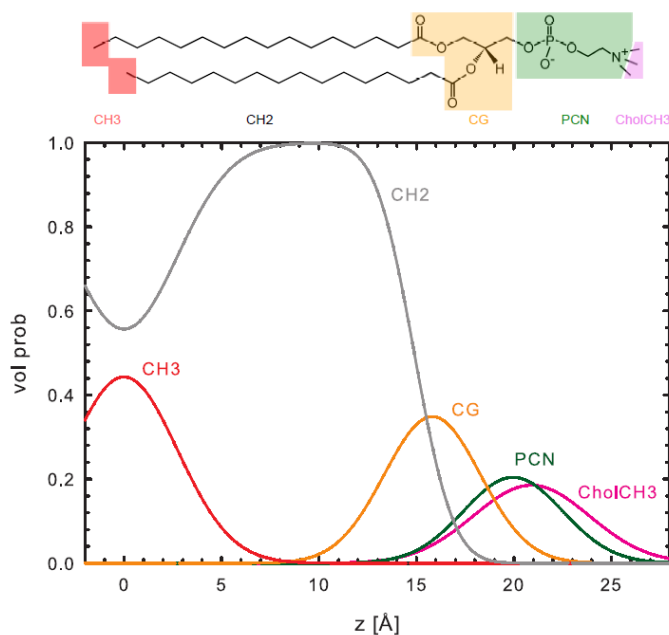

Figure 3.11: Parsing scheme for DPPC (Adapted from [10])

The parsing scheme (as shown for DPPC in Figure 3.11) models the lipids by using Gaussians to describe the different groups, CH_3, CH_2, CG, PCN and $Cholesterol - CH_3$. In the former program the lipid bilayer was only divided into headgroups and tails and therefore fewer different Gaussians were used [26].

SDP-GAP is an optimization program based on a genetic algorithm. Depending on data originating from scattering experiments, models are optimized to minimize the quadratic deviation to the measured values. Thereby several structural parameters, such as the bilayer thickness or the lateral area per lipid, are evaluated.

There were two additional steps performed before the fitting process. First, a polynomial background was subtracted in addition to the water background. This was especially useful for the nano domains because the program is constructed in a way that the minima in the scattering curves are all set to the same level when working in the nanoscopic regime. Second, the errorbars in selected sections of the data were changed, to force the fit to a more accurate compliance in these segments.

The results that were calculated with this program for nanoscopic domains (A1-A5) are all similar to the one shown in Figure 3.12, where the optimized model (black) and the underlying data (green) are compared for A1.
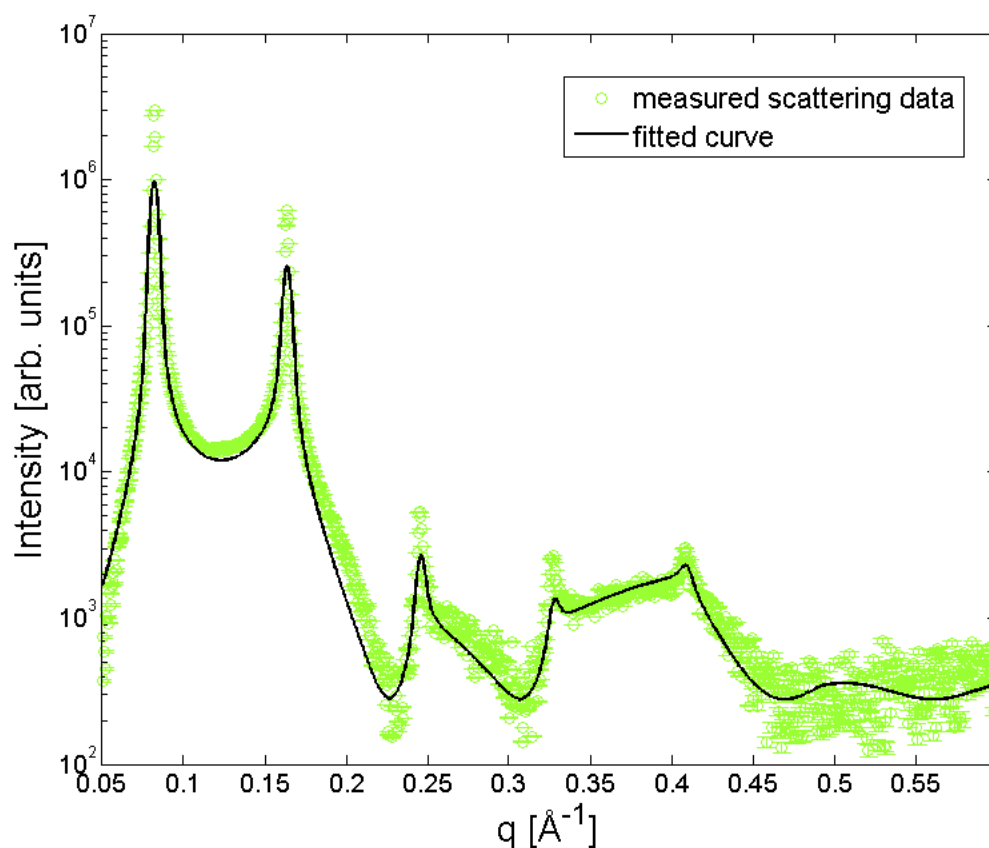
Figure 3.12: Fit for A1 ($\rho_{DOPC} = 0\%$) received by the SDP-GAP program (black) compared to the original data (green)

The fact that there are no double peaks in the scattering curve suggests the appearance of domains in the nanoscopic range. In other words, the domains are not large enough for being resolved by x-ray scattering and not aligned in the different bilayers within the multilamellar vesicles. For these reasons a discrimination between the two fluid phases by their d-spacings is not possible from the scattering data.

The models that were determined with this program for macroscopic domains (A6-A17) looked similar to the one in Figure 3.13 for A17.
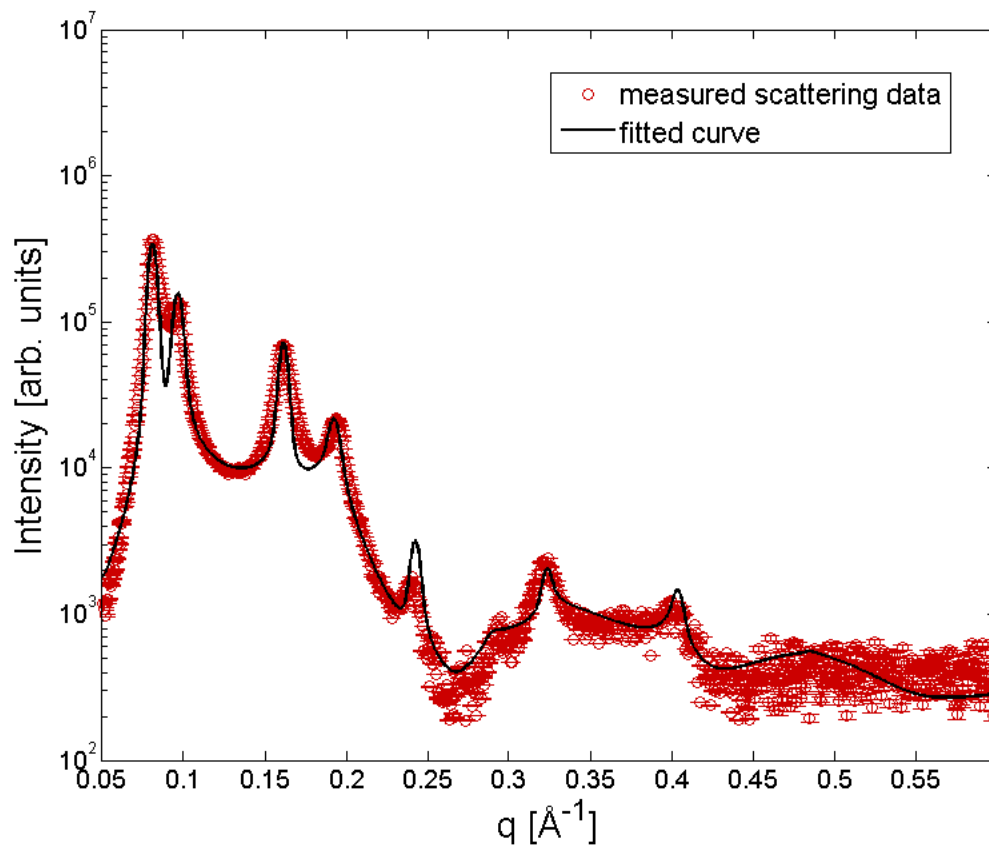
Figure 3.13: Fit for A17 ($\rho_{DOPC} = 100\%$) received by the SDP-GAP program (black) compared to the original data (red)

The Bragg peaks for two different d-spacings that can clearly be told apart in Figure 3.13 originate from the phase separation into macro domains.

The d-spacings calculated by the program for the different lipid compositions are illustrated depending on their DOPC content in Figure 3.14, where the black line represents the d-spacings of nano domains, the red (L_o) and blue line (L_d) the d-spacings of the macro domains.
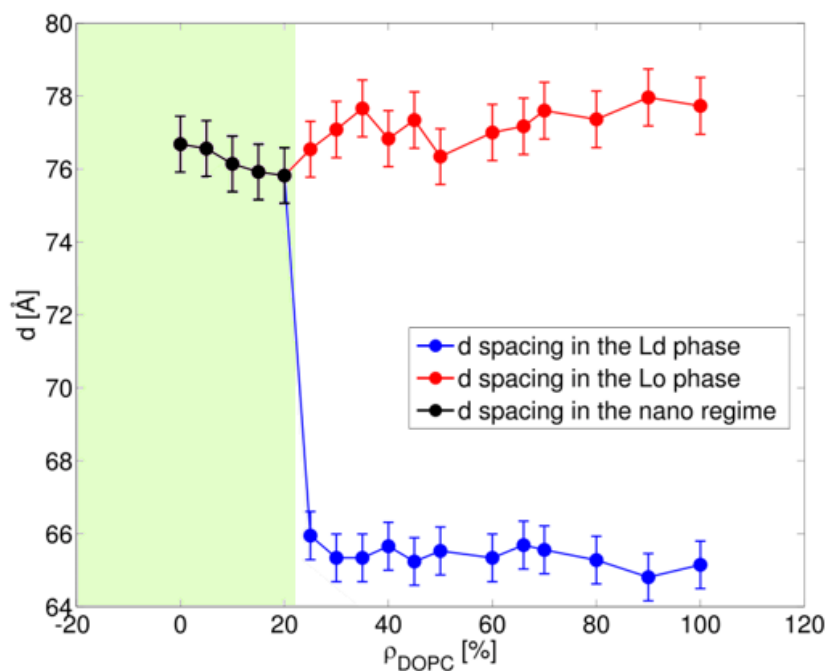
Figure 3.14: d-spacings of different DSPC/DOPC/POPC/Cholesterol samples depending on their composition

Nano domains occur at a DOPC/POPC ratio of up to $\rho_{DOPC} = 20$ %. The values of the d-spacings are between 75 and 77 Å.

Above a DOPC/POPC ratio of $\rho_{DOPC} = 25$ % there are two different d-spacings for every sample. The higher one (between 76 and 78 Å) is the d-spacing of the L_o phase, where the higher amount of cholesterol has an ordering effect on the lipids, which thickens the bilayer. The lower one (between 64 and 66 Å) is the d-spacing of the L_d phase which is less ordered and more than 10 Å thinner than the L_o phase. The fact that the d-spacings of the nano domains are closer to the L_o than to the L_d phase is another indicator for the existence of domain structure and not a pure liquid disordered phase like it occurs above a certain transition temperature (see sec. 3.1).

Within the nano range, the d-spacing seems to be slightly decreasing with increasing DOPC content, whereas in the macro regime the d-spacings remain more or less constant despite the further increase of ρ_{DOPC}.

The program also calculated the bilayer thickness d_B, which is only the thickness of the lipid bilayer itself without the intermediate water layers ($d_B = d - d_W$) (see Figure 1.16). It is displayed in Figure 3.15.
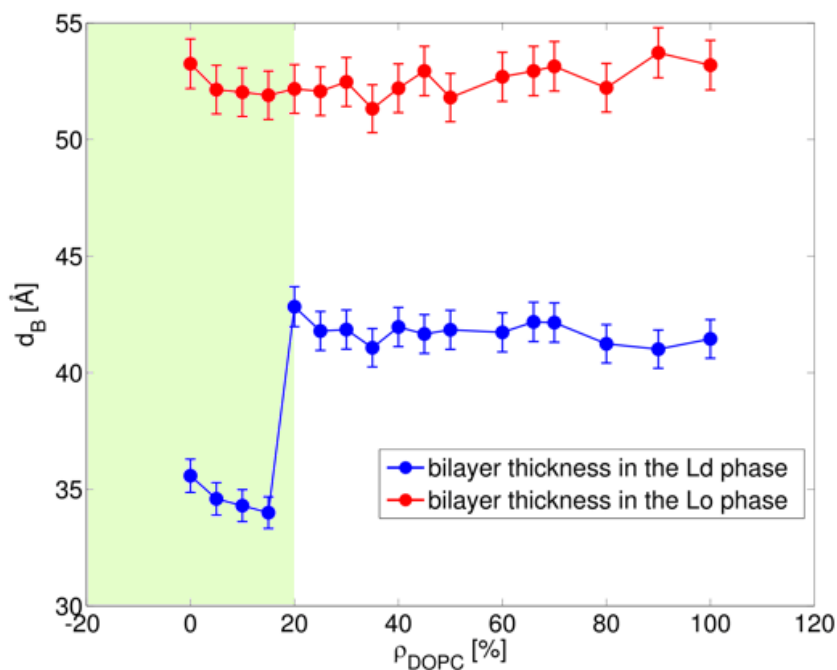
Figure 3.15: Bilayer thicknesses of different DSPC/DOPC/POPC/Cholesterol samples depending on their composition

The difference in the bilayer thicknesses of the two phases was expectable. For the same reason as for the d-spacings, the liquid ordered phase is thicker than the liquid disorded phase for the macroscopic domains.

However, the behavior in the nano regime raises questions. The fact that the program generates values for the bilayer thicknesses in nano domains that are further

apart from each other for the two different phases than the ones for macro domains is physically questionable as previous results have shown a smaller difference between the d-spacings of the phases in the nanoscopic regime [10]. It is conjecturable that the L_d phase is laterally squeezed by the L_o phase in the nanoscopic regime, resulting in an increased bilayer thickness of the L_d phase. An explanation for the oppositional behavior gained from this program could be the calculation of the form factor without a cross-term, the fixation of the volumes beforehand and the subtraction of an artificial background.

Another calculated parameter is the area per lipid, which is defined as the lateral area of the headgroups per lipid molecule. Its dependency on the DOPC content is shown in Figure 3.16.
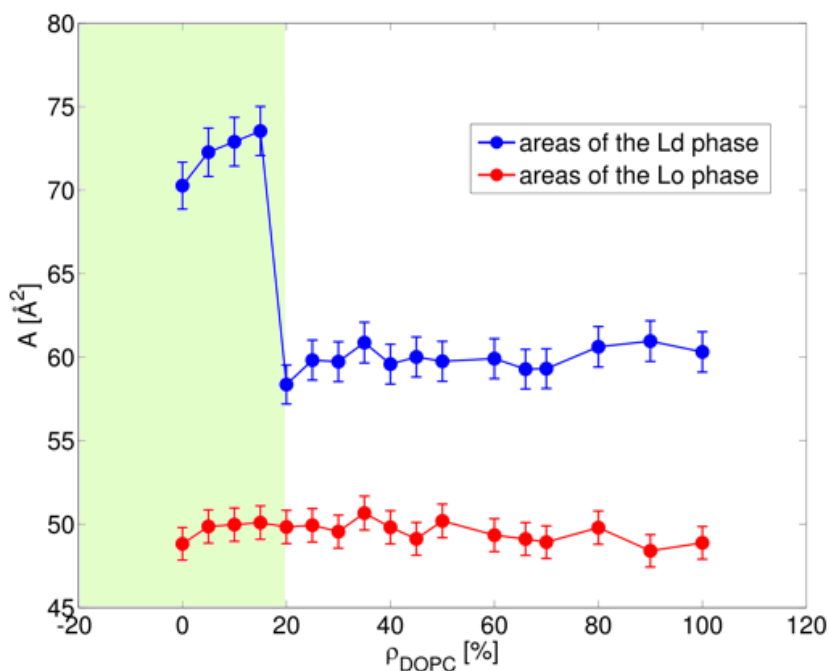

Figure 3.16: Lateral areas per lipid of different DSPC/DOPC/POPC/Cholesterol samples depending on their composition

In the macro regime, the areas remain somewhat constant with the L_d areas (57-61 Å^2) being about 8-12 Å^2 bigger than the L_o areas (48-51 Å^2), which is reasonable because the lipids in the liquid disordered phase are less stiff and therefore their head-groups move around to a greater extent and engage more space. In the nanoscopic regime, the areas for the L_o phase are about the same as in the macroscopic regime, but the areas for the L_d phase seem to become bigger. This behavior is oppositional to what would physically be expected as the areas should be more similar to each other in the nanoscopic regime [10]. The reason for this expectation is, that the area per lipid (A) is calculated from the volume of the whole lipid (V_{lipid}) divided by the bilayer thickness (d_B), making it inversely proportional to d_B (see Eq.3.2).

$$d_B \propto \frac{V_{lipid}}{A} \tag{3.2}$$

The lateral squeezing of the L_d phase that was already mentioned before, leads to a reduction of the areas per lipid for the L_d phase.

The oppositional behavior resulting from this program is again ascribed to the subtraction of an artificial background and the use of a form factor without a cross-term among others.

The fluctuations in the lipid bilayer are represented by η (the Caillé parameter). It is a function of temperature, the bilayer bending modulus (K_C) and the bulk modulus of interbilayer compression (B) as shown in Equation 3.3.

$$\eta \propto \frac{T}{\sqrt{K_C B}} \tag{3.3}$$

The calculated values for the Caillé parameter are plotted in Figure 3.17.
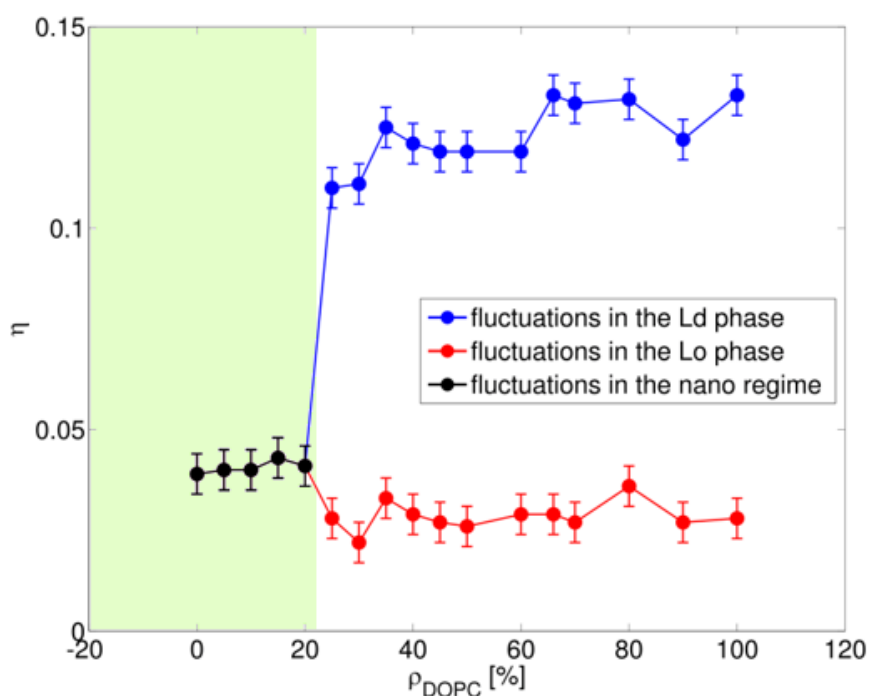
Figure 3.17: Bilayer fluctuations of different DSPC/DOPC/POPC/Cholesterol samples depending on their composition

In the nano regime the fluctuations are about 0,04, in the macro regime they split up into the fluctuations in the L_o phase (0,02-0,04) and the fluctuations in the L_d phase (0,11-0,14). The higher values of the fluctuations in the liquid disordered phase can be attributed to its less ordered and therefore more flexible form. The low values in the nano regime (almost like the ones in the L_o phase) indicate a predominantly ordered liquid structure.

Similar systems were measured and modelled by P. Heftberger et al. [10]. The values in the macroscopic regime are in good agreement with data received in this work, whereas the behavior in the nanoscopic regime differs, presumably due to an unstable algorithm.

3.2.2 Analysis with the 'SAXSMLV' program

The same samples were modeled with another Global Analysis Program for SAXS measurements of MLVs, developed by M. Belička in 2016 (Belička et al., in preparation). It is also based on the SDP (Scattering Density Profile) model [17] but it differs from the SDP-GAP program in section 3.2.1 in several points. An advantage is the use of two form factors in the nanoscopic regime and the application of crossed form factors, thus the subtraction of polynomials was not necessary.

Representatively for the optimized models from this program for nanoscopic domains, the fits and the original data for A1 are compared in Figure 3.18.

Figure 3.18: Fit for A1 ($\rho_{DOPC} = 0\%$) received by the SAXSMLV program (black) compared to the original data (green)

The fit stays within the errorbars of the original data almost through the whole range. Most notably, the first order peaks are approximated better with this program when compared to Figure 3.12 because an exponential distribution was chosen for representing the number of bilayers in the stack instead of a Gaussian distribution (see Eq. 3.4).

$$f(N; N_{mean}) = \frac{1}{N_{mean}} \ e^{-\frac{N}{N_{mean}}} \tag{3.4}$$

N represents the number of bilayers, N_{mean} the mean number of bilayers.

The optimized models from this program for macroscopic domains are represented by A17 for which the fit is compared to the original data in Figure 3.19.
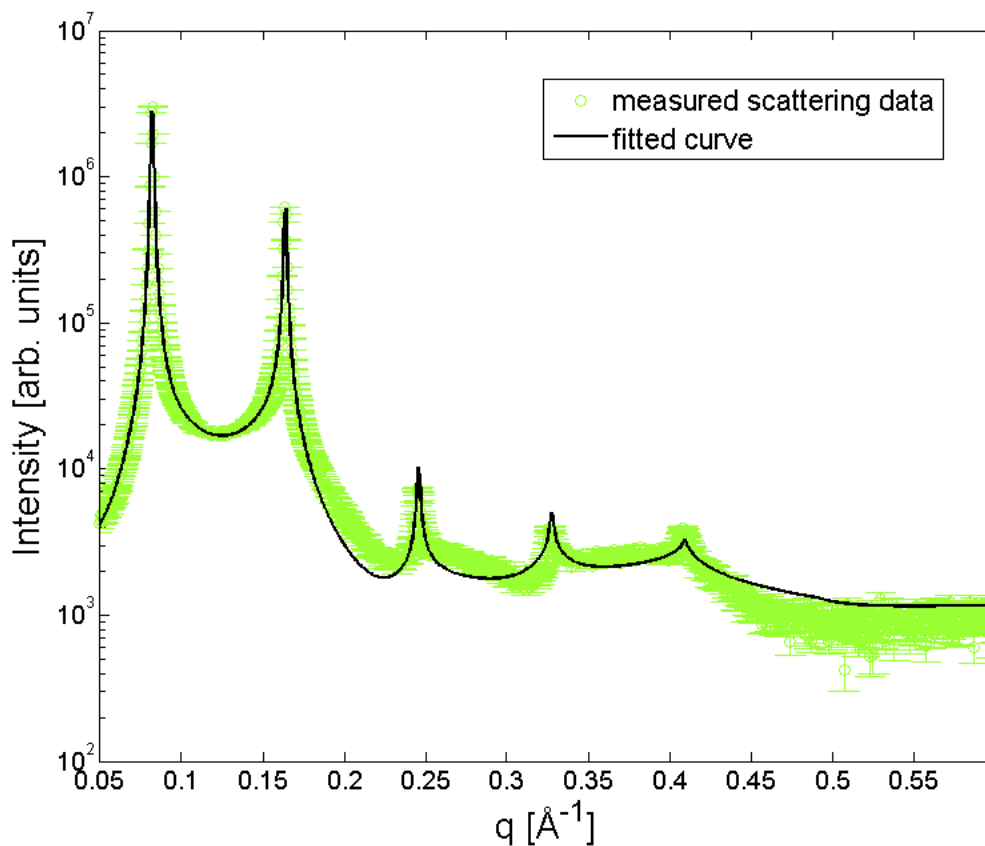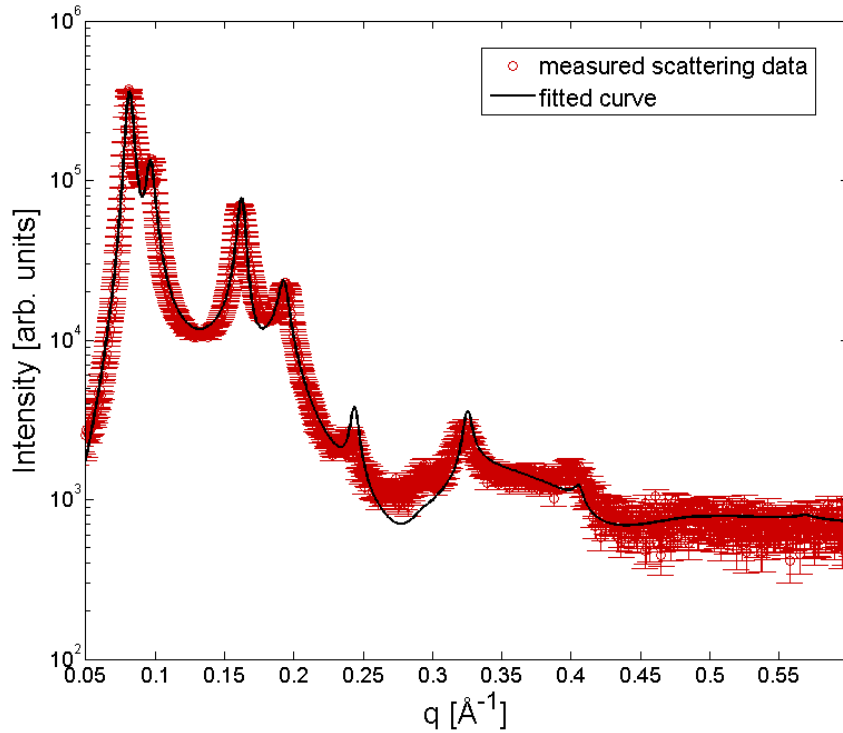

Figure 3.19: Fit for A17 ($\rho_{DOPC} = 100\%$) received by the SAXSMLV program (black) compared to the original data (red)

The dependency of the d-spacing on the DOPC content is shown in Figure 3.20.
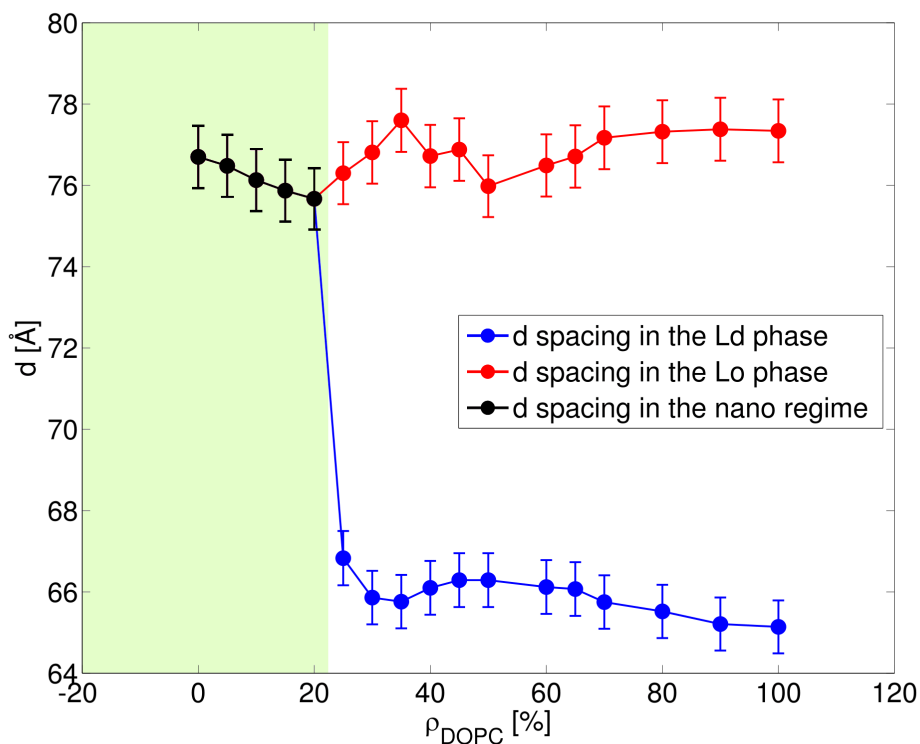
Figure 3.20: d-spacings of different DSPC/DOPC/POPC/Cholesterol samples depending on their composition

It looks rather similar to the plot received from the SDP-GAP program (Figure 3.14) again with a common d-spacing in the nanoscopic range and a split-up into two d-spacings for the two phases in the macroscopic range.

The bilayer thickness was also calculated by the SAXSMLV program and is illustrated in Figure 3.21.
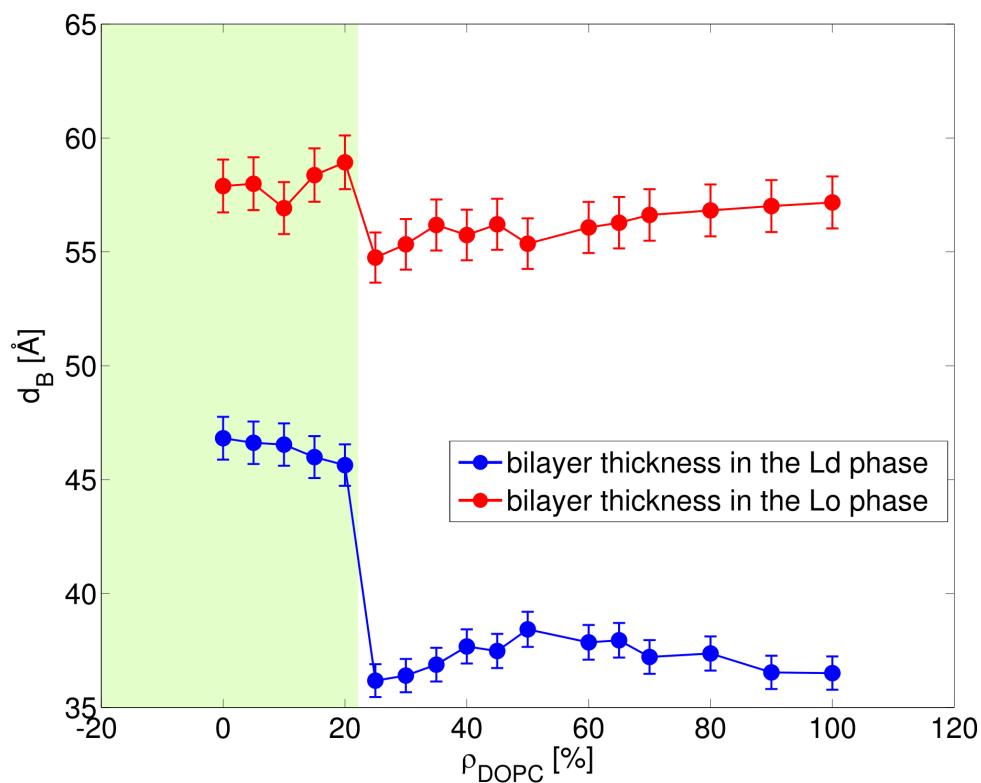
Figure 3.21: Bilayer thicknesses of different DSPC/DOPC/POPC/Cholesterol samples depending on their composition

Compared to the bilayer thicknesses calculated with the SDP-GAP program (Fig. 3.15) the curves clearly differ, not only in their form but also in their magnitude. The bilayer thicknesses calculated with SAXSMLV in the macroscopic range differ more strongly for the two phases (15-20 Å instead of roughly 10 Å). They also display a different behavior in the nanoscopic regime. While the L_o phase appears to remain more or less the same as for macroscopic domains, the bilayer thickness in the L_d phase is several Å larger for nano domains, which is the opposite behavior than the one calculated with SDP-GAP (see sec. 3.2.1). The fact that the bilayer thicknesses are closer together in the nanoscopic range is physically more realistic as the lateral

squeezing of the L_d phase by the L_o phase causes higher bilayer thicknesses of the L_d phase. This theory was also supported by the measurement and fitting of the L_d phase endpoint of the DSPC/POPC/Chol. tieline at 20°C (Figure 3.22).
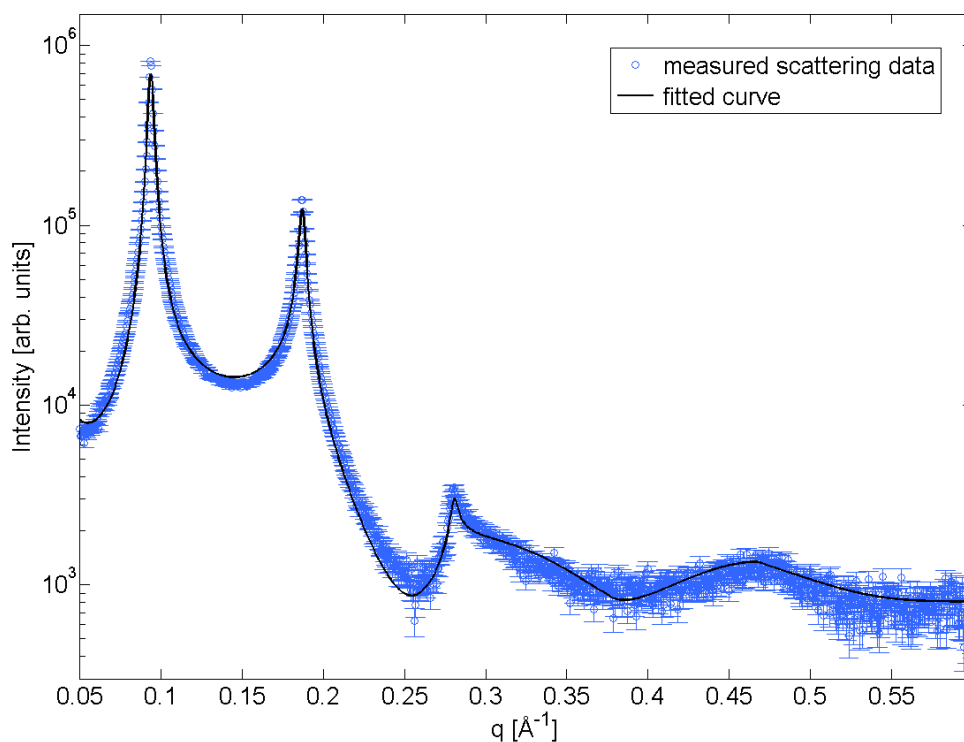
Figure 3.22: Scattering curve of the pure L_d phase endpoint sample E1 (DSPC/POPC/Chol. = 0,09/0,79/0,12)

The calculated bilayer thickness ($d_B \approx 42,5$ Å) is thinner than d_B of the coexisting L_d phase in the nanoscopic regime ($d_B \approx 46,5$ Å), implying a thickening caused by the L_o phase.

The calculated areas for the different sample compositions are illustrated in Figure 3.23.
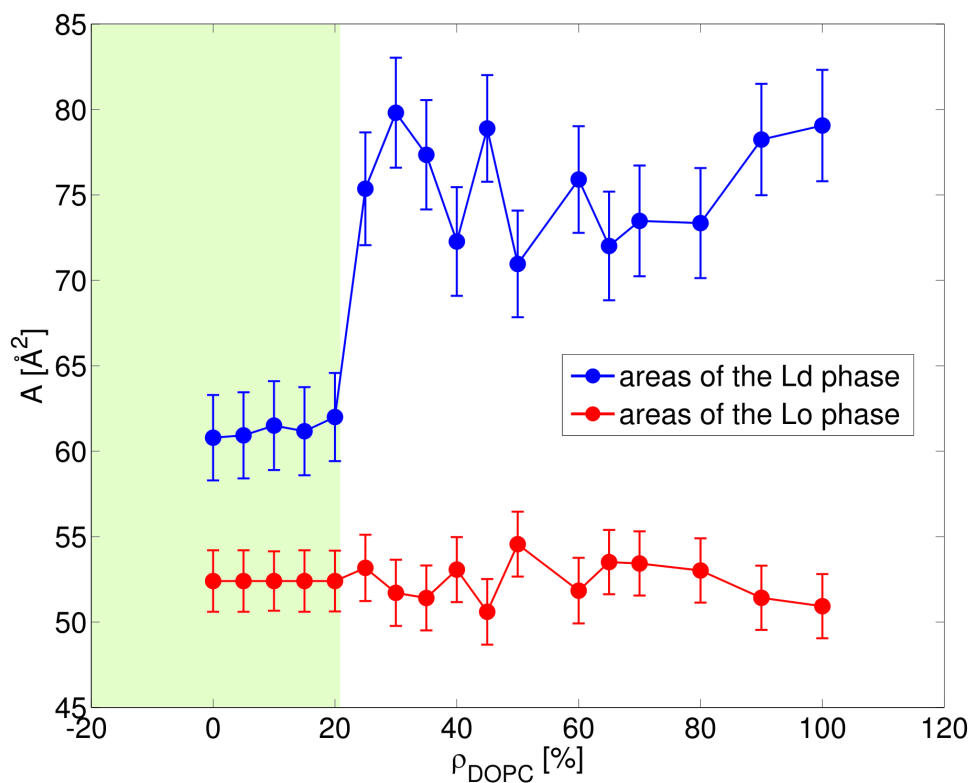
Figure 3.23: Lateral areas per lipid of different DSPC/DOPC/POPC/Cholesterol samples depending on their composition

The areas for the macro domains vary quite a lot between 70 and 80 Å^2 within the L_d phase and between 50 and 55 Å^2 in the L_o phase. This behavior is ascribable to the soft constraints for the volumes of the lipids as the areas depend on them. They were not fixed to a certain value but part of the fitting process with a small scope of about 30 Å^3. For the nano domains the areas of the L_o phase were fixed to the average of the value for the macro domains (52,4 Å^2) as they should not change significantly depending on the composition because the DOPC respectively the POPC lipids are

mainly part of the L_d phase. The areas for the L_d phase remained almost constant, between 60 and 62 Å^2, within the nanoscopic regime. Compared to the areas determined from the SDP-GAP program the values are quite similar to each other for the L_o phase (they only differ by about 3 Å^2). The discrepancies occur in the L_d phase, where values for macro domains received from SAXSMLV are 10-20 Å^2 higher than the ones calculated by SDP-GAP. A reason for this deviation might be the different methods of calculating the areas by the two programs. In the nano regime the behavior of the areas for the L_d phase shows opposed characteristics to the one calculated before. The areas in the nano domains compared to the macro domains appear to be smaller (ΔA = 10 - 20 Å^2) for the SAXSMLV program and bigger (ΔA = 10 - 15 Å^2) in the SDP-GAP program. The results received from the SAXSMLV program seem to be more realistic, because it physically makes sense that the differences of the areas in the nanoscopic range are smaller because the L_d phase is squeezed by the L_o phase. The calculated model for the tieline endpoint (Fig. 3.22) provided a lateral area per lipid of $A \approx 62,9$ Å^2, showing the decrease of the area per lipid in the nanoscopic coexisting L_d phase ($A \approx 60,5$ Å^2) due to the influence of the L_o domains.

The bilayer fluctuations depending on the DOPC content gained from this program show similar behavior as already seen in Figure 3.17, but with an even more stable course. They are displayed in Figure 3.24.
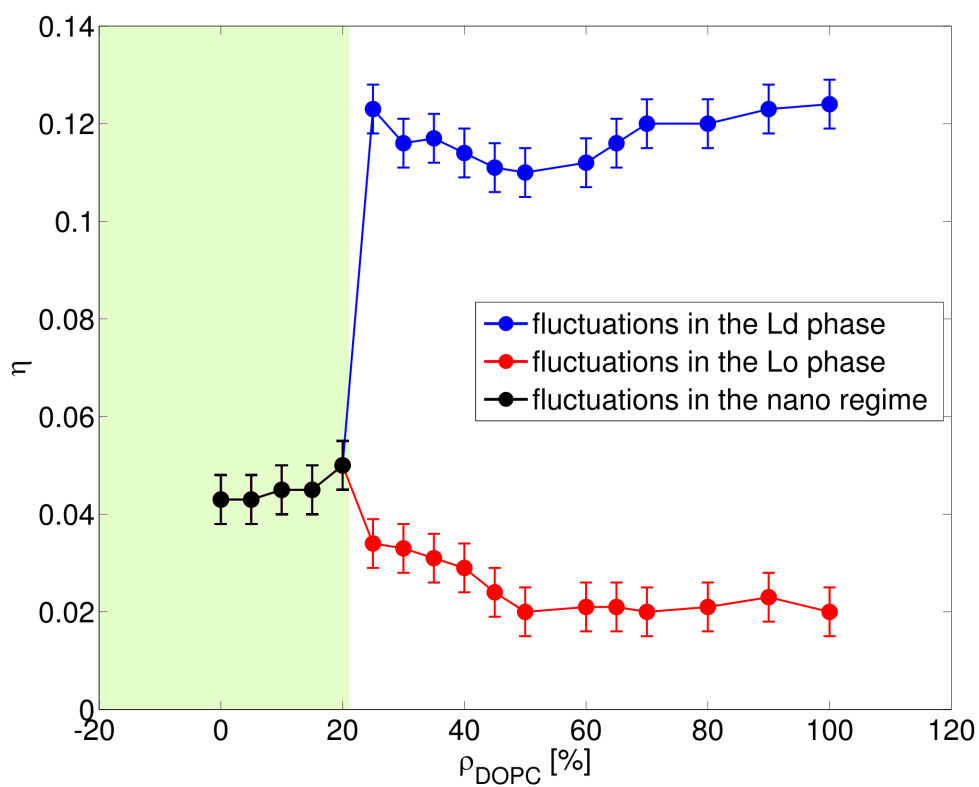
Figure 3.24: Bilayer fluctuations of different DSPC/DOPC/POPC/Cholesterol samples depending on their composition

Another output of the program is the creation of electron density profiles for the two phases separately. A general case of an electron density profile compared to the lipid bilayer is illustrated in Figure 1.16. The profiles generated from the program for nano respectively macro domains are shown in Figures 3.26 and 3.25.
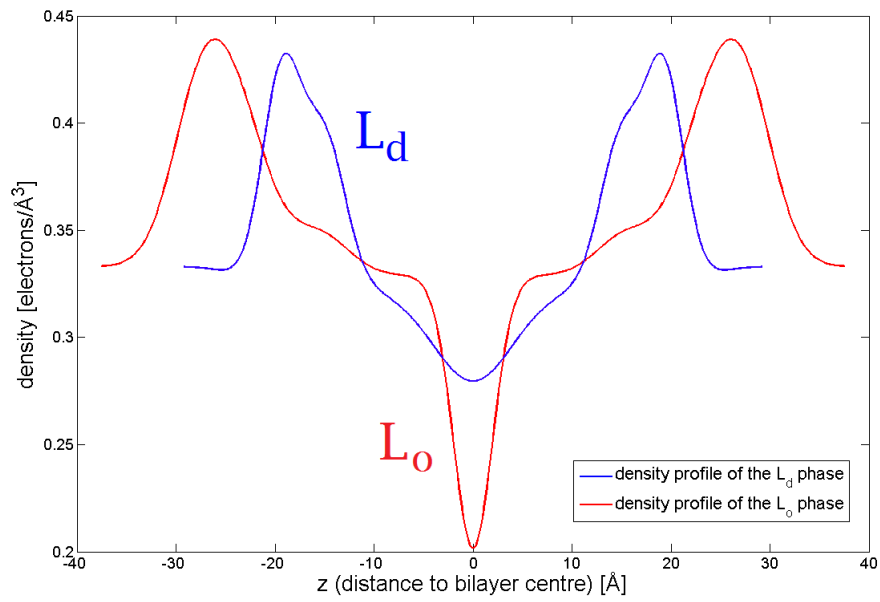
Figure 3.25: Electron density profiles for A17 (macroscopic regime)
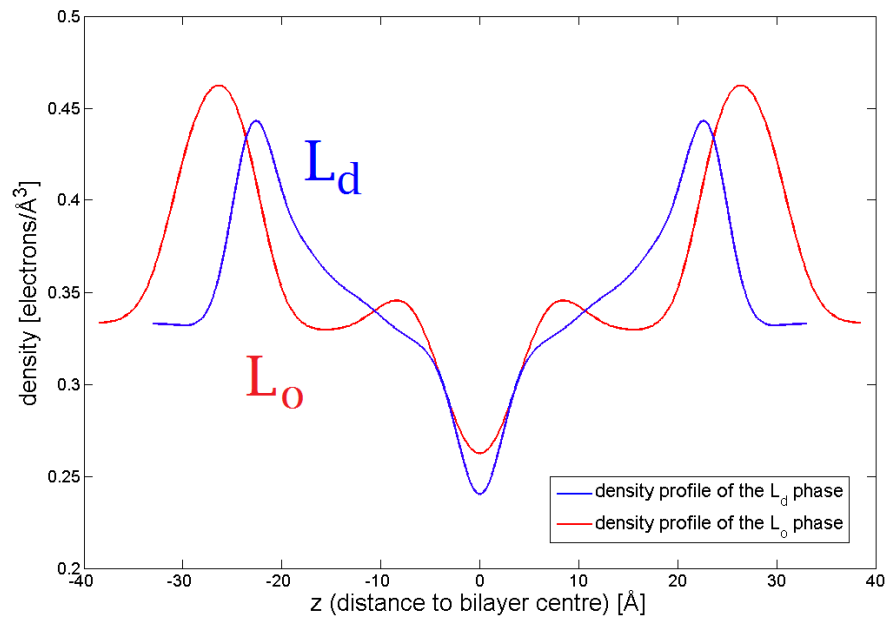
Figure 3.26: Electron density profiles for A1 (nanoscopic regime)

When viewing a lipid bilayer along its normal, the electron density profile depends on z, the distance to the bilayer center. The electron density is high at the headgroups, decreases in the section of the chains and reaches a minimum at the terminal methyl groups of the chains. This behavior also applies when splitting the electron density profile into the ones for the two different phases L_d and L_o.

The profile for macroscopic domains in Figure 3.25 shows that the maxima of the liquid ordered phase are further apart than the ones for the liquid disordered phase, which was expected as the L_o phase is thicker and therefore the distance between the headgroups is larger. At the center of the bilayer, the electron density is lower for the L_o phase as it is more stiff and ordered and therefore the ends of the chains are more straightened. For the L_d phase the electron density in the center is higher because the chains are more flexible.

The profile for nanoscopic domains in Figure 3.26 shows the same behavior concerning the distance of the headgroups but in the center of the bilayer the electron densities are almost the same for both phases. This can be explained by the fact that the differences in the phases are bigger in the macroscopic regime.

3.3 Contourplots

To graphically compare the different examined transitions, Figure 3.27 shows contour plots of the data collected for different temperatures (left) and for different compositions (right) with their corresponding scattering curves.
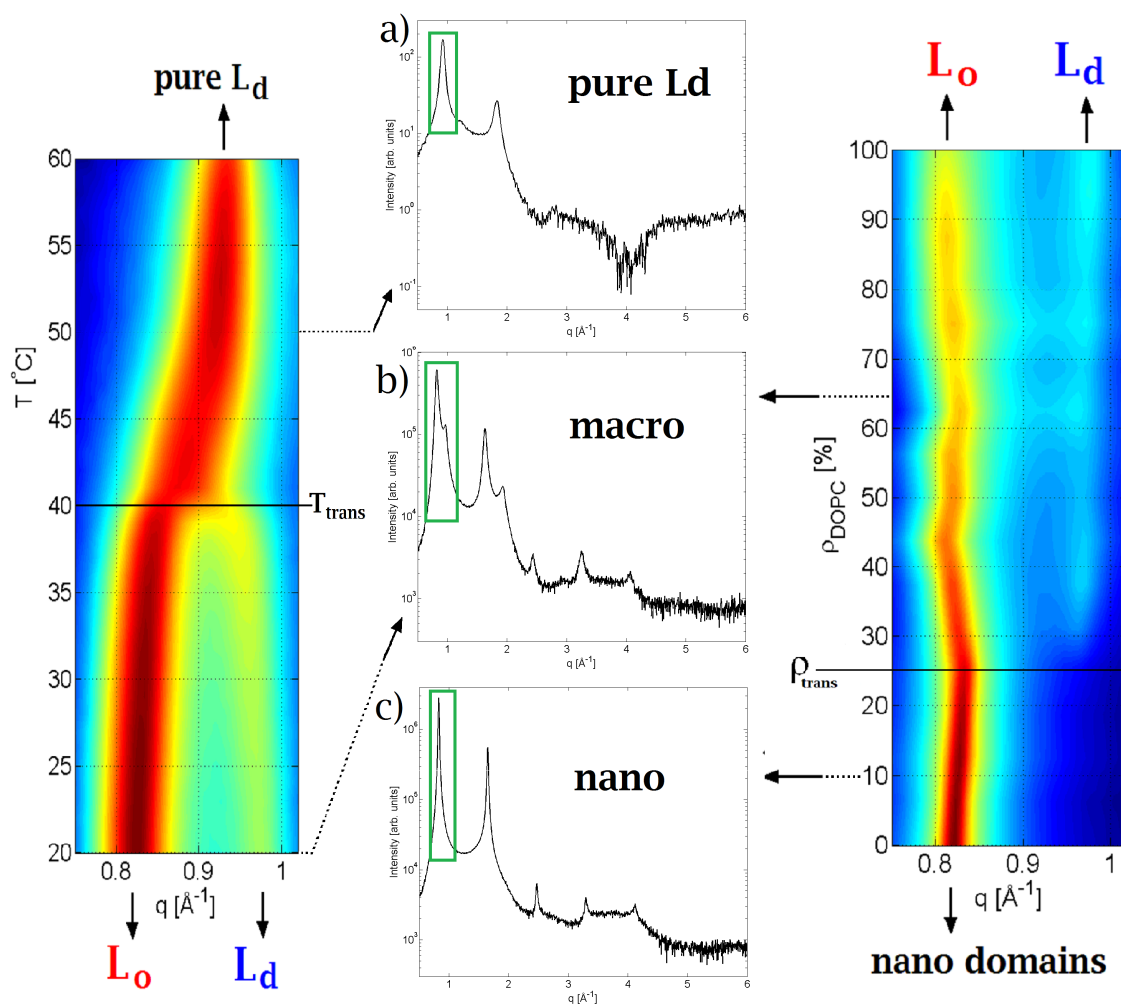

Figure 3.27: Comparison of the two examined transitions via contourplots: melting of the L_o domains at a certain transition temperature (left), transition from macro to nano domains at a certain DOPC/POPC ratio (right), corresponding scattering curves (middle)

The contour plot for a DOPC/POPC ratio of $\rho_{DOPC} = 65\%$ for different temperatures collected in 1°C steps shows the relation between the scattering vector, q, the temperature and the scattering intensity, which is represented by different colors - blue displays low intensities and red high intensities. The separation into L_o and L_d domains at temperatures up to 40°C and the melting into a pure L_d phase above this transition temperature is clearly observable.

The corresponding scattering curves are the upper two (a) and b)). The first one shows a measurement of the given composition at 50°C whereas the second one originates from the measurement of the same sample at 20°C. The detail of the scattering curves used for both contour plots was the sector between 0,75 and 1,02 Å^{-1}, where the first order peaks appear.

The contour plot on the right side of Figure 3.27 shows the transition between nano and macro domains at a constant temperature of 20°C with changing composition. At high DOPC/POPC ratios, where ρ_{DOPC} is above 25%, the two phases can be distinguished, with the L_o phase Bragg peak at about 0,82 Å^{-1} and the L_d phase peak at about 0,97 Å^{-1}. At low DOPC/POPC ratios, only one first order peak is observable at roughly the same scattering vector as the L_o phase of the macro domains.

The corresponding scattering curves are the two lower ones (b) and c)). Scattering curve b) was collected for a sample composition of $\rho_{DOPC} = 65\%$, scattering curve c) represents a DOPC/POPC ratio of $\rho_{DOPC} = 10\%$.

Chapter 4

Conclusion

This work investigated transition processes depending on temperature and composition in four component lipid-only mixtures.

SAXS and DSC measurements on DSPC/DOPC/POPC/Cholesterol mixtures of different DOPC/POPC ratios showed a temperature-induced melting of the L_o phase of the phase separated domain structure, leading to a homogeneous L_d phase. The transition temperature for this process was thereby dependent on the sample composition. For macroscopic domains, a shift of the transition temperature to higher values with increasing DOPC content was found, that followed a linear trend. In the nanoscopic regime, the transition temperature did not perceptibly vary with changing sample composition.

The d-spacings, obtained from SAXS measurements at varied temperatures, showed different values for coexisting L_d and L_o phases below the transition temperature and one d-spacing for the homogeneous L_d phase above the melting temperature of the domain structure. The height mismatch between the d-spacings of the different phases below the transition temperature followed a 2-dimensional Ising model.

SAXS measurements at a constant temperature showed the dependency of the domain size on the DOPC/POPC ratio. Below $\rho_{DOPC} = 25\%$, scattering curves only showed Bragg-Peaks for one d-spacing, above this ratio, two different d-spacings could be distinguished, suggesting a nanoscopic domain structure below and a macroscopic one above this critical DOPC/POPC ratio.

Further parameters could be obtained by using two recently developed SDP-GAP programs for multilamellar vesicles to construct models describing the collected scattering data. Thereby d-spacings, bilayer thicknesses, lateral areas per lipid and bilayer fluctuations were obtained among others.

The behavior of these parameters in the nanoscopic regime suggested a squeezing effect, where the lateral areas per lipid of the L_d phase were compressed by the L_o phase and depending on that, the bilayer thicknesses of the L_d phase were increased. Furthermore, electron density profiles were obtained, for the different phases separately, in the nanoscopic as well as in the macroscopic regime.

Within the framework of this thesis, only sample compositions following one of a huge number of tielines were examined, leaving a lot of work to survey more of parameter space in future investigations.

Bibliography

[1] *eukaryote: animal cell.* Encyclopædia Britannica Online. 2008.

[2] D. G. Ackerman and G. W. Feigenson. Lipid bilayers: clusters, domains and phases. *Essays in biochemistry*, 57:33–42, 2015.

[3] M. Aktas, L. Danne, P. Möller, and F. Narberhaus. Membrane lipids in agrobacterium tumefaciens: Biosynthetic pathways and importance for pathogenesis. *Frontiers in Plant Science*, 5(109), 2014.

[4] B. Alberts. *Essential cell biology.* Garland Science, New York, 3rd ed. edition, 2010.

[5] D. W. Ball, J. W. Hill, and R. J. Scott. Introduction to chemistry: General, organic, and biological (v. 1.0), 2011.

[6] M. Eeman and M. Deleu. *From biological membranes to biomimetic model membranes.* Les Presses agronomiques de Gembloux, 2010.

[7] F. A. Heberle and G. W. Feigenson. Phase separation in lipid membranes. *Cold Spring Harb Perspect Biol*, 3(4):a004630, 2011.

[8] F. A. Heberle, R. S. Petruzielo, J. Pan, N. Drazba, P.and Kučerka, R. F. Standaert, G. W. Feigenson, and J. Katsaras. Bilayer thickness mismatch controls domain size in model membranes. *Journal of the American Chemical Society*, 135(18):6853–6859, 2013.

[9] F. A. Heberle, J. Wu, S. L. Goh, R. S. Petruzielo, and G. W. Feigenson. Comparison of three ternary lipid bilayer mixtures: FRET and ESR reveal nanodomains. *Biophys J*, 99(10):3309–3318, 2010.

[10] P. Heftberger. *Structure and elasticity of fluid membrane domains.* Phd thesis, 2015.

[11] P. Heftberger, B. Kollmitzer, F. A. Heberle, J. Pan, M. Rappolt, H. Amenitsch, N. Kučerka, J. Katsaras, and G. Pabst. Global small-angle x-ray scattering data analysis for multilamellar vesicles: the evolution of the scattering density profile model. *Journal of Applied Crystallography*, 47(Pt 1):173–180, 2014.

[12] P. Heftberger, B. Kollmitzer, A. Rieder, H. Amenitsch, and G. Pabst. In situ determination of structure and fluctuations of coexisting fluid membrane domains. *Biophysical Journal*, 108(4):854–862, 2015.

[13] A. Hodzic, M. Rappolt, H. Amenitsch, P. Laggner, and G. Pabst. Differential modulation of membrane structure and fluctuations by plant sterols and cholesterol. *Biophysical Journal*, 94(10):3935–3944, 2008.

[14] I. V. Ionova, V. A. Livshits, and D. Marsh. Phase diagram of ternary cholesterol/palmitoylsphingomyelin/palmitoyloleoyl-phosphatidylcholine mixtures: Spin-label EPR study of lipid-raft formation. *Biophys J*, pages 1856–1865, 2012.

[15] H. Jakubowski. *Biochemistry Online: An Approach Based on Chemical Logic.* iLumina, Wilmington, N.C., 2002.

[16] T. M. Konyakhina, J. Wu, J. D. Mastroianni, F. A. Heberle, and G. W. Feigenson. Phase diagram of a 4-component lipid mixture: DSPC/DOPC/POPC/chol. *Biochim Biophys Acta*, 1828(9):2204–2214, 2013.

[17] N. Kucerka, J. F. Nagle, J. N. Sachs, S. E. Feller, J. Pencer, A. Jackson, and J. Katsaras. Lipid bilayer structure determined by the simultaneous analysis of neutron and x-ray scattering data. *Biophys J*, 95(5):2356–2367, 2008.

[18] E. Lafer. Membrane lipids I and II: Glycerophospholipids and sphingolipids, December 6, 2011.

[19] A. L. Lehninger. *Biochemistry*. Worth, (New York, N.J.), (6. print) edition, 1972.

[20] D. Marquardt, B. Geier, and G. Pabst. Asymmetric lipid membranes: towards more realistic model systems. *Membranes*, 5(2):180–196, 2015.

[21] D. Marquardt, F. A. Heberle, J. D. Nickels, G. Pabst, and J. Katsaras. On scattered waves and lipid domains: detecting membrane rafts with x-rays and neutrons. *Soft Matter*, 2015.

[22] O. G. Mouritsen. *Life - as a matter of fat: The emerging science of lipidomics.* Frontiers collection. Springer, Berlin, 2005.

[23] O. G. Mouritsen. Lipids, curvature, and nano-medicine. *European journal of lipid science and technology : EJLST*, 113(10):1174–1187, 2011.

[24] J. D. Nickels, X. Cheng, B. Mostofian, C. Stanley, B. Lindner, F. A. Heberle, S. Perticaroli, M. Feygenson, T. Egami, R. F. Standaert, J. C. Smith, D. A. A. Myles, M. Ohl, and J. Katsaras. Mechanical properties of nanoscopic lipid domains. *Journal of the American Chemical Society*, 137(50):15772–15780, 2015.

[25] G. Pabst. Biologische und biobasierte Materialien, 2015.

[26] G. Pabst, R. Koschuch, B. Pozo-Navas, M. Rappolt, K. Lohner, and P. Laggner. Structural analysis of weakly ordered membrane stacks. *J Appl Crystallogr*, 36:1378–1388, 2003.

[27] J. A. Pople. Everything you ever wanted to know about SAXS but were afraid to ask, 2008.

[28] M. C. Rheinstädter. Collective molecular dynamics in proteins and membranes (review). *Biointerphases*, 3(2):FB83, 2008.

[29] A. Rieder. *Aufbau und Optimierug einer Rapid Solvent Exchange Apparatur zur Herstellung künstlicher Zellmembranen.* Master thesis, Juni, 2014.

[30] K. A. Riske, R. P. Barroso, C. C. Vequi-Suplicy, R. Germano, V. B. Henriques, and M. T. Lamy. Lipid bilayer pre-transition as the beginning of the melting process. *Biochimica et biophysica acta*, 1788(5):954–963, 2009.

[31] E. Sackmann and R. Merkel. Strukturuntersuchung mit Kleinwinkelstreuung, 2011.

[32] H. Schäfer. *Elektromagnetische Strahlung: Informationen aus dem Weltall*, volume 1 of *Astronomie*. Vieweg, Braunschweig [u.a.], 1985.

[33] H. Schnablegger and Y. Singh. *The SAXS Guide: Getting acquainted with the principles.* Austria, 2013.

[34] E. J. Shimshick and H. M. McConnell. Lateral phase separation in phospholipid membranes. *Biochemistry*, 12(12):2351–2360, 1973.

[35] K. Simons and E. Ikonen. Functional rafts in cell membranes. *Nature*, 387(6633):569–572, 1997.

[36] S. J. Singer and G. L. Nicholson. The fluid mosaic model of the structure of cell membranes. *Science*, 175:720–731, 1972.

[37] J. Sochor, B. Ruttkay-Nedecky, Hubalek-J., Babula-P., R. Kizek, and V. Adam. *Automation of Methods for Determination of Lipid Peroxidation.* INTECH Open Access Publisher, 2012.

[38] P. Uppamoochikkal, S. Tristram-Nagle, and J. F. Nagle. Orientation of tie-lines in the phase diagram of DOPC/DPPC/cholesterol model biomembranes. *Langmuir*, 26(22):17363–17368, 2010.

[39] C. J. van Oss, H. Visser, and W. Norde. *50 years of DLVO theory*, volume v. 14, no. 1-4 of *Colloids and surfaces. B, Biointerfaces.* Elsevier, Amsterdam and New York, 1999.

[40] R. Winter. Struktur und Dynamik von Modell-Biomembranen. *Chemie in unserer Zeit*, 24(2):71–81, 1990.